Analysis and Design of Axisymmetric Transonic Flow with Linearized Three-Dimensional Flow Prediction

by

Jon Ahn

B.S., Seoul National University, Korea, 1986
M.S., Seoul National University, Korea, 1988

Submitted to the Department of Aeronautics and Astronautics
in partial fulfillment of the requirements for the degree of

Doctor of Philosophy

at the

MASSACHUSETTS INSTITUTE OF TECHNOLOGY

February 1997

Author..............
Department of Aeronautics and Astronautics
January 27, 1997

Certified by ....
Professor Mark Drela
Department of Aeronautics and Astronautics
Thesis Supervisor

Certified by ....
Professor Kenneth Breuer
Department of Aeronautics and Astronautics

Certified by ....
Professor Alan H. Epstein
Department of Aeronautics and Astronautics

Accepted by....
Professor Jaime Peraire
Chairman, Department Graduate Committee

Analysis and Design of Axisymmetric Transonic Flow with Linearized Three-Dimensional Flow Prediction

by

Jon Ahn

Submitted to the Department of Aeronautics and Astronautics
on January 27, 1997, in partial fulfillment of the
requirements for the degree of
Doctor of Philosophy

Abstract

An axisymmetric transonic viscous flow analysis and design method has been developed by applying stream-surface based Newton method. This method incorporates a linearized three-dimensional flow prediction capability, using a linear perturbation of the axisymmetric solution. Euler equations are coupled with axisymmetric integral boundary equations with two-dimensional closure and transition models. Stream-surface based finite volume formulations allow efficiency and useful design features. An actuator disk is used to model the fan disk inside a powered nacelle. A stream-surface grid generation scheme using a panel method has been developed to provide an adequate initial grid. Comparisons are made to analytic solutions and wind tunnel experiments of nacelles, resulting in good agreements. The algorithm shows fast convergence, typically within 10 iterations.

Thesis Supervisor: Professor Mark Drela
Department of Aeronautics and Astronautics

Acknowledgments

Doing something at MIT had been my dream during youth years, but I never thought that would be such a long stay. I owe thanks through lifetime to my wife Donghee who endured and supported all those years while raising two beautiful children, Jiyoung and Yoolip to whom I owe lost playtimes and talks. Also, I'm deeply indebted to my parents and parents in law, who encouraged and supported their beloved children toward higher education without hesitation.

It has been a worldclass experience to hang around Mark Drela (☙) who inspired every word on this thesis. I once read an author wrote, "Nothing in this thesis can be claimed to be the author's own", and now I find myself in the same situation. Prof. Epstein deserves special thanks for supporting with his expertise in this field and the research materials that could not be obtained otherwise. No less gratitude goes to Prof. Breuer, Prof. Mcmanus, Prof. Greitzer, Dr. Tan of GTL, and Dr. Lord of Pratt & Whitney, who have provided with helpful thoughts and never failed to encourage me.

Also, I can not skip the nice people of FDRL and its predecessors (CASL, CFDL). Bob Haimes and Steve Ellis supported with computing resources during my early years. Angie, Ed, and Tolulope saved me from recent system problems during the lab merger and system upgrades. Ali, Brian(now at Boeing), Bilal, Folusho, Josh, and Tom shared all the toils, pains, and laughs. Mike pleased us with treats like mass-scale Jello.

Faith is one of the best things that I found during MIT years and it has been my guiding light. I thank Reverend Won-Joon Yim, Korean Hope Church, Gate Bible Study, and Lunch Prayer Group, who have shared the joy and encouraged each other with prayers.

Lastly, I can not appreciate too much the people who made my MIT dream possible with financial supports. This research has been funded by Korean Government Scholarship, MIT Dean of Engineering via Soderberg Career Development Chair, and by Korean Air, in the order received. Especially, I thank Mr. Yi-Taek Shim and Dr. Si-Yoong Ryu of Korean Air for their sincere support on this research which seemed to never end.

Contents

3

List of Figures

5

Nomenclature

Roman Symbols

A_1, A_2	back, front bounding vectors
A_g	meridian angle peturbation
A_n	cell cross-sectional area
B^+, B^-	upper, lower bounding vectors
C	annular wing chord
C_D	dissipation coefficient
C_f	friction coefficient
$C_{L\alpha}$	lift coefficient slope
C_n	linearized 3D pressure correction coefficient
$C_n p$	linearized 3D pressure correction
C_τ	shear stress coefficient
D	cell width vector
E, K	complete elliptic integral of the second, first kind
H	shape parameter
H^*	energy thickness shape parameter
H^{**}	density thickness shape parameter
H_k	kinematic shape parameter
I	design object function
L	cowl length
M	Mach number
M_c	upwind switching Mach number
N	qusi-normal cell vector
P_e	exit pressure
Q	general vector
R	general vector function
Re_θ	boundary layer Reynolds number
S	streamwise cell vector

S_{LE}	leading edge stagnation point location
U	free stream speed
U_e	boundary layer edge velocity
a, b, f, g	cell geometric factor
g	design mode shape
h_t	stagnation enthalpy
$\vec{i},\ \vec{j},\ \vec{k}$	unit vectors
m	mass flow of streamtube
m_k	mass flow of flow passage
n	stream-surface location
$\tilde{n}$	amplification factor, design mode amplitude
$\bar{n}$	body surface location
p	pressure
p_c	pressure correction
q	streamwise speed, general variable
q_∞	free stream dynamic pressure
s	cell geometric factor
$u,\ v$	induced potential velocity
w	swirl velocity
$x,\ y$	coordinates
y_o	potential ring radius
y_e	boundary layer edge radius

Indices

$I2$	outflow boundary i index
ILE	leading edge i index
$J2$	farfield boundary j index
JT	j index of streamtube with shifted equation
L	design mode numer

NX	$I2 - 1$
NY	number of streamtubes
i, j	computational domain index
k	flow passage index

Subscripts

$+, -, 0, 1, 2, 3$	location in conservation cell
∞	free stream
a	algebraic average
$comp, incomp$	compressible, incompressible flow
e	boundary layer edge value
n	quasi-normal vector component
s	source ring
t	stagnation quantity
v	vortex ring
x, y	x, y component of vector

Superscripts

$+/-$	upper/lower conservation cell surface
$*$	throat
A	axisymmetric flow value
ec	eccentric mode
m	Newton cycle level
t	stagnation quantity
x, y	x, y component of vector
$'$	perturbed variable

Greek Symbols

Δ	jump across actuator disk
Σ	source ring strength
Γ	vortex ring strength
α	angle of attack
γ	specific heat ratio, vortex sheet strength
δ	correction variable
δ^*, δ^{**}	displacement, density thickness
κ	pressure correction coefficient
λ	upwind switching function, aspect ratio
ϕ	induced potential, meridian angle
π^+, π^-	pressure on upper, lower surface
ρ	density
θ, θ^*	mometum, kinetic energy thickness
τ	shear stress
ξ, η	boundary layer coordinate

Acronyms

CPU	central processing unit
FDM	finite difference method
MFR	mass flow ratio

Chapter 1

Introduction

The research of civil jet propulsion systems in the last half a century has been driven by the need for reliable, efficient, light, quiet, economic, and clean burning engines. High bypass ratio turbofan engines introduced in the late 60's marked a step jump in most criteria, and ever since, bypass ratio has been increased to the point that weight and drag penalties from bigger engine nacelles begin to outweigh their benefits. Accordingly, the aerodynamic performance of the nacelle itself has become very important, compared to its traditional and primary role of airflow supplier to the engine. But, due to the high degree of interaction between nacelle and engine, traditional part by part design and matching procedures have seen more shortcomings recently, necessitating capabilities to analyze the whole nacelle flowfield while modeling the chief functions of an engine correctly, which are addition of energy and mass. Still, even with leaping advances being made in computers and numerical schemes, a full numerical simulation of an engine belongs far in the future due to the complexity and the size of such a computation.

To overcome this, various efforts have been made to analyze the nacelle flow with a physical model simulating the essential features of the fan, which interacts directly with the nacelle. Ealier works and some of recent works by Chen *et al.* [11], Uenishi *et al.* [51], and Iek *et al.* [26] relied on specified boundary conditions on the surface of the fan disk. More recently, several methods using a simple but successful modeling of the fan as an actuator disk with energy and pressure jump were introduced by Pankajashan *et al.* [39], Leicher [33], Knight *et al.* [29]. The actuator disk modeling has been widely used in the simulation

of the interaction phenomena between the engine inlet flow and a compressor blade row, and the interaction between multistage compressor blade rows (Tan [49], Greitzer [23], Joo [27]).

Actuator disk modeling has several benefits over the former. One is that the parameters of the actuator disk are translated directly into physical fan parameters. Also, radial quilibrium is achieved everywhere, even across the fan, allowing useful applications like spanwise fan blade designs. Joo [27] went one step further to distribute the fan strength over multiple actuator disks through the width of fan disk , relieving the level of discontinuity per disk and thus better modeling the fan. The author feels that numerical problems which have accompanied specified boundary condition modeling of a fan may be a sign that some of the fan flow physics are missing, and thus , actuator disk modeling is a better representation of a fan.

But, even with a simple modeling of the fan, three-dimensional analysis/design of nacelle is still costly, taking about 1 hour of CPU on the CRAY-YMP for an Euler solution of engineering accuracy. For Navier-Stokes codes of Iek *et al.* [26], and Uenishi *et al.* [51] , it takes about 40-80 hours. This CPU requirement is effectively preventing designers from investigating various designs in initial design stages.

An axisymmetric design code can cut a portion of these expensive calculations by providing a better designed base axisymmetric geometry, from which most three-dimensional designs start. Also, its smaller computing resource requirements can allow designers to try many various design concept and configurations. The number can be further cut down by a research tool with a capability to predict three-dimensional flow within permissable level of approximation while maintaining computational efficiency.

In two-dimensional flow, Drela [17] and Giles [19] introduced a novel stream-surface based approach to transonic analysis/design problems. The stream-surface grid itself is a part of the solution, which endows versatile surface design capabilities at a little extra cost. And the coupling of integral boundary layers allows the result to match viscous results of Navier-Stokes solvers at a fraction of CPU. Not surprisingly, the resulting Newton solver called ISES has found various applications with productive results, especially in airfoil designs. Although there have been a few other Newton approaches by Edwards and McRae

[18], Orkwis and McRae [38], and Venkatakrishnan [52], none of them comes close to the design versatilities and fast solution process of ISES.

The primary goal of this thesis is the application of the proven stream-surface based Newton method to anlysis/design of an axisymmetric nacelle with the actuator disk modeling of a fan. And to futher utilize the benefits of the Newton method, full attention is given to the linearized prediction of three-dimensional flow from a base axisymmetric solution, with an aim at replacing costly three-dimensional flow computations during initial nacelle design stages. The resulting code is to be called AMIS (Axisymmetric Multiple-passage Interacting Stream-surface Euler solver) to denote the lineage of Newton solver family pioneered by Drela and Giles, although AMIS has been built from scratch and share a few code lines.

The following chapter of this thesis present the development of the stream-surface based axisymmetric Newton solver along with pratical issues. Chapter 3 covers the extension of the axisymmetric work to the linearized three-dimensional prediction method. Following are the computational results for validation, and exploration of the capabilities of the overall analysis/design approach. Finally, Chapter 6 closes this thesis with conclusions and recommendations.

Chapter 2

Axisymmetric Flow Theory

In this chapter, governing equations and their discretized forms are derived for axisymmetric non-swirling transonic flows, along with proper boundary conditions and their discretizations. The first three sections describe the Euler equation for inviscid flow modeling and integral boundary layer equations for viscous boundary layer modeling, accompanied by their coupling relations. The fourth section covers proper boundary conditions which make the problem well-posed. The fifth section discusses the actuator disk modeling of a fan. Following those, Newton solution procedures and global variable definitions precede stream-surface grid generation method. Finally, description of the design method closes this chapter.

2.1 Euler equations

The inviscid transonic flow is governed by steady Euler equations which are given in integral forms.

Continuity Equation :

$$\oint \rho(\vec{q} \cdot \vec{n}) dA = 0 \tag{2.1}$$

Momentum Equation :

$$\oint [\rho(\vec{q} \cdot \vec{n})\vec{q} + p\vec{n}] dA = 0 \tag{2.2}$$

Energy Equation :

$$\oint \rho(\vec{q} \cdot \vec{n}) h_t dA = 0 \tag{2.3}$$

2.2 Finite volume formulations

2.2.1 Conservation cell

Discretized Euler equations are formulated through bookeeping of flux and pressure balances on the finite volume cell as shown in Figure 2-2 as the area wrapped by vectors A_1, A_2, B^+, and B^-. All flow variables are defined at the cell center, as shown in Figure 2-1, except pressure π^+, and π^-, which are defined at the centers of upper and lower conservation surfaces. q_1, q_2 are scalar speeds in the direction of streamwise vectors S_1, S_2.

By defining the conservation cell between six grid points along stream surfaces, Drela [17] took all the merits of grid point centered method while keeping the simplicity of the cell centered method. All flow variables needed to apply conservation laws are clearly defined on conservation cell surfaces, eliminating typical averaging of most cell centered schemes. For clear understanding of axisymmetric conservation cells, perspective view of surface 1 is shown in Figure 2-3. Upper (+), lower (-), front (2), and back (1) surface areas are dependent on the local radius y. For example, the back area is found as $|A_1 \times D_1|$, where $D_1 = y_1 \, d\phi \, \vec{k}$.

Note that y is used as the radius from the symmetric axis. Useful vectors and factors are defined in Equations (2.4) - (2.8).
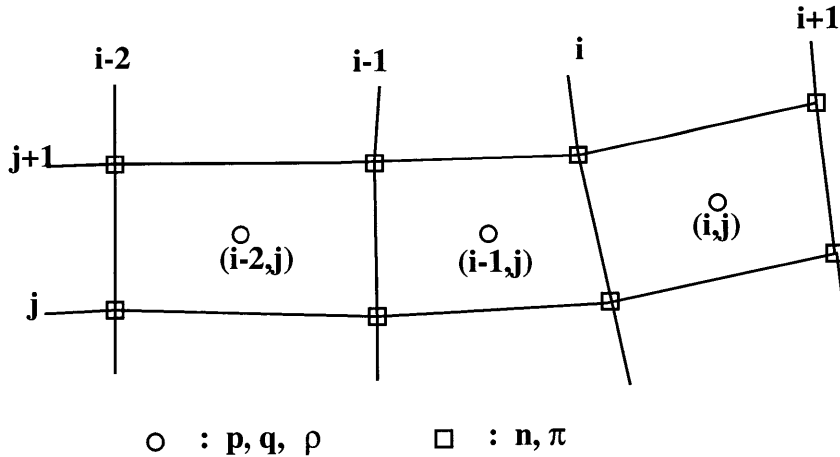
Figure 2-1: Points of flow variable definition
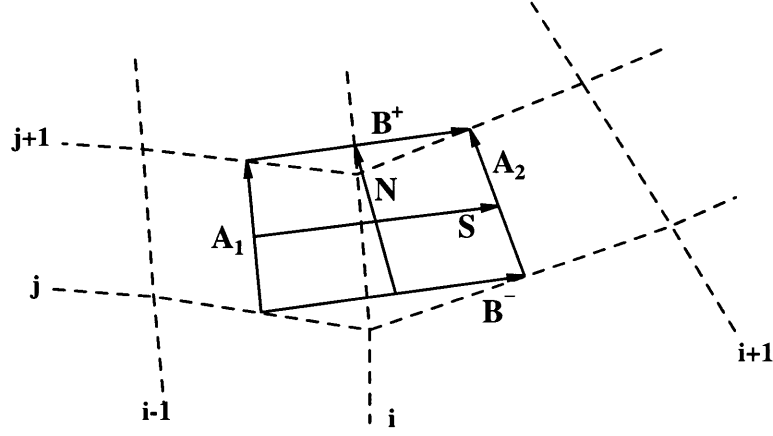
Figure 2-2: Conservation cell and bounding vectors

Definitions of non-dimensional S_1, S_2 vectors :

$$dx_1 = \tfrac{1}{2}(x_{i,j} + x_{i,j+1} - x_{i-1,j} - x_{i-1,j+1}), \quad dy_1 = \frac{1}{2}(y_{i,j} + y_{i,j+1} - y_{i-1,j} - y_{i-1,j+1}),$$

$$s_1 = \sqrt{{dx_1}^2 + {dy_1}^2}, \quad s_{x1} = \tfrac{dx_1}{s_1}, \quad s_{y1} = \tfrac{dy_1}{s_1}, \quad S_1 = s_{x1}\vec{i} + s_{y1}\vec{j} \tag{2.4}$$

$$dx_2 = \tfrac{1}{2}(x_{i+1,j} + x_{i+1,j+1} - x_{i,j} - x_{i,j+1}), \quad dy_2 = \frac{1}{2}(y_{i+1,j} + y_{i+1,j+1} - y_{i,j} - y_{i,j+1})$$

$$s_2 = \sqrt{{dx_2}^2 + {dy_2}^2}, \quad s_{x2} = \tfrac{dx_1}{s_1}, \quad s_{y2} = \tfrac{dy_1}{s_1}, \quad S_2 = s_{x2}\vec{i} + s_{y2}\vec{j} \tag{2.5}$$

Definitions of $+/-$ vectors (Figure 2-4) :

$$
\begin{aligned}
S_1{}^+ &= (x_{i,j+1} - x_{i-1,j+1})\vec{i} & + \quad (y_{i,j+1} + y_{i-1,j+1})\vec{j} \\
S_2{}^+ &= (x_{i+1,j+1} - x_{i,j+1})\vec{i} & + \quad (y_{i+1,j+1} + y_{i,j+1})\vec{j} \\
S_1{}^- &= (x_{i,j} - x_{i-1,j})\vec{i} & + \quad (y_{i,j} + y_{i-1,j})\vec{j} \\
S_2{}^- &= (x_{i+1,j} - x_{i,j})\vec{i} & + \quad (y_{i+1,j} + y_{i,j})\vec{j} \\
b_x{}^+ &= \tfrac{1}{2}(x_{i+1,j+1} - x_{i-1,j+1}) \;, & b_y{}^+ &= \tfrac{1}{2}(y_{i+1,j+1} - y_{i-1,j+1}) \qquad (2.6) \\
b_x{}^- &= \tfrac{1}{2}(x_{i+1,j} - x_{i-1,j}) \;, & b_y{}^- &= \tfrac{1}{2}(y_{i+1,j} - y_{i-1,j}) \\
B^+ &= b_x{}^+\vec{i} + b_y{}^+\vec{j} \;, & B^- &= b_x{}^-\vec{i} + b_y{}^-\vec{j} \\
s_x &= b_x{}^+ + b_x{}^- \;, & s_y &= b_y{}^+ + b_y{}^+ \\
S &= \tfrac{1}{2}(B^+ + B^-)
\end{aligned}
$$

15
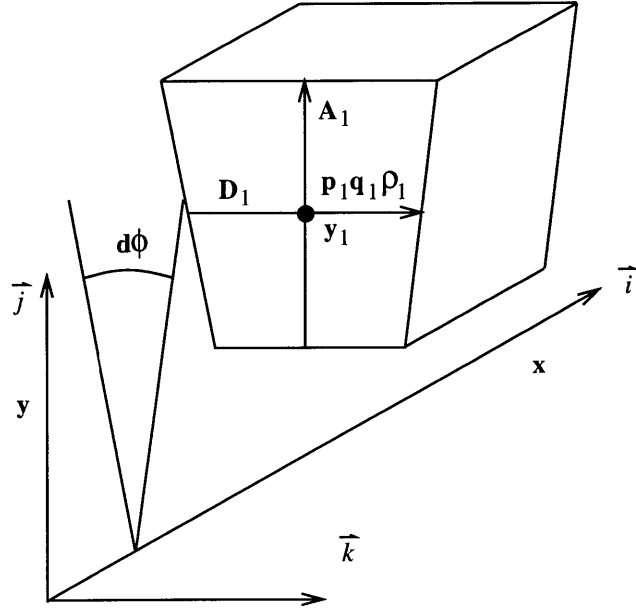
Figure 2-3: Perspective view of conservation cell back surface

Definitions of N, A_1, A_2 vectors :

$$a_{x1} = \tfrac{1}{2}(x_{i-1,j+1} + x_{i,j+1} - x_{i-1,j} - x_{i,j}) \ , \quad a_{y1} = \tfrac{1}{2}(y_{i-1,j+1} + y_{i,j+1} - y_{i-1,j} - y_{i,j})$$

$$a_{x2} = \tfrac{1}{2}(x_{i,j+1} + x_{i+1,j+1} - x_{i,j} - x_{i+1,j}) \ , \quad a_{y2} = \tfrac{1}{2}(y_{i,j+1} + y_{i+1,j+1} - y_{i,j} - y_{i+1,j})$$

$$x_n = \tfrac{1}{2}(a_{x1} + a_{x2}) \ , \qquad\qquad\qquad y_n = \tfrac{1}{2}(a_{y1} + a_{y2})$$

$$A_1 = a_{x1}\vec{i} + a_{y1}\vec{j} \ , \quad A_2 = a_{x2}\vec{i} + a_{y2}\vec{j} \ , \qquad N = \tfrac{1}{2}(A_1 + A_2)$$

$$(2.7)$$

Definitions of radii on conservation cell surfaces :

$$y_1 = \tfrac{1}{4}(y_{i-1,j} + y_{i,j} + y_{i-1,j+1} + y_{i,j+1}), \quad y_2 = \tfrac{1}{4}(y_{i,j} + y_{i+1,j} + y_{i,j+1} + y_{i+1,j+1})$$

$$y^+ = \tfrac{1}{4}(y_{i-1,j+1} + 2y_{i,j+1} + y_{i+1,j+1}), \qquad y^- = \tfrac{1}{4}(y_{i-1,j} + 2y_{i,j} + y_{i+1,j})$$

$$(2.8)$$

2.2.2 Discretized equations

The beauty of the stream surface based finite volume formulation is the simplified equations, allowing reduction in the number of variables per cell, that is, continuity equation and energy equation become algebraic identities and can be dropped out. Their simplicity allows simple modeling of energy and mass flow addition which happen to be primary functions of an jet engine. With the help of Equations (2.4) - (2.8), conservation laws Equations (2.1)-(2.3)

16
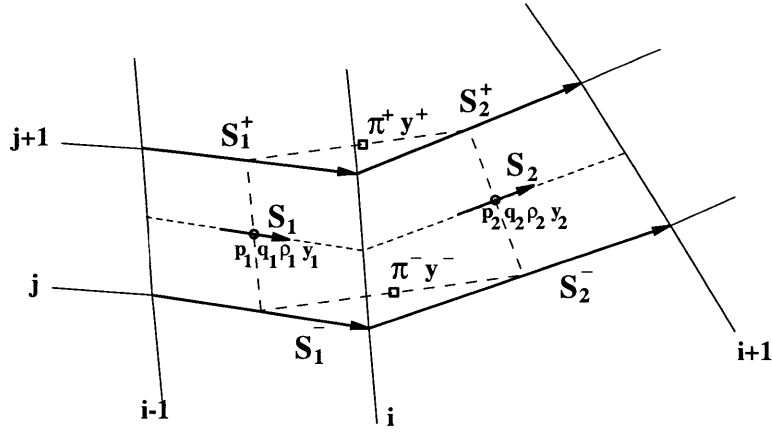
Figure 2-4: Definition of streamwise vectors

are transformed into discretized forms given by Equations (2.9)-(2.12). Presence of pressure terms from side faces in Equation (2.11) and the dependence of face area changes on radius are the main features that differentiate the present axisymmetric flow formulations from the two-dimensional formulations.

Continuity equation :

$$m \quad = \quad \rho_1 q_1 A_{n1} \quad = \quad \rho_2 q_2 A_{n2}$$

$$\text{where} \quad A_{n1} = S_1 \cdot (A_1 \times y_1 \vec{k}), \quad A_{n2} = S_2 \cdot (A_2 \times y_2 \vec{k}) \tag{2.9}$$

x-momentum equation (axial) :

$$mq_1 s_{x1} - mq_2 s_{x2} + p_1 a_{y1} y_1 - p_2 a_{y2} y_2 + \pi^+ b_y^+ y^+ - \pi^- b_y^- y^- = 0 \tag{2.10}$$

y-momentum equation (radial):

$$mq_1 s_{y1} \quad - \quad mq_2 s_{y2} + p_1 a_{x1} y_1 - p_2 a_{x2} y_2 - \pi^+ b_x^+ y^+ + \pi^- b_x^- y^-$$

$$+ \quad \frac{1}{2} |S \times N| (p_1 + p_2) = 0 \tag{2.11}$$

17

Energy equation :

$$h_{t\infty} = \frac{\gamma}{\gamma - 1}\frac{p_1}{\rho_1} + \frac{1}{2}q_1{}^2 = \frac{\gamma}{\gamma - 1}\frac{p_2}{\rho_2} + \frac{1}{2}q_2{}^2 \tag{2.12}$$

2.2.3 S-momentum and N-momentum equations

Following the algebra suggested in Drela [17] and with the addition of pressure correction to prevent saw-tooth mode of grids, S-momentum and N-momentum equations are obtained.

Pressure correction :

$$\pi^+ y^+ + \pi^- y^- = p_1 y_1 + p_2 y_2 + p_c(y_1 + y_2) \tag{2.13}$$

$$p_c = \kappa\gamma(p_1 + p_2)M^2 \cdot \frac{|S_1{}^- \times S_2{}^-| - |S_1{}^+ \times S_2{}^+|}{s_1 s_2} \tag{2.14}$$

A typical value $\kappa = 0.025$ is effective for most transonic flow problems.

S-momentum equation :

$$\begin{aligned}
s_x(2.10) + s_y(2.11) \quad &= \\
mq_1 f_1 - mq_2 f_2 \quad &+ \quad (p_1 - p_2)\frac{(y_2 + y_1)}{2} + p_c\frac{|B^- \times B^+|}{|S \times N|}\frac{(y_2 + y_1)}{2} = 0 \\
&\text{where } f_1 = \frac{S_1 \cdot S}{|S \times N|}, \quad f_2 = \frac{S_2 \cdot S}{|S \times N|}
\end{aligned} \tag{2.15}$$

N-momentum equation :

$$\begin{aligned}
x_n(2.10) + y_n(2.11) \quad &= \\
mq_1 g_1 - mq_2 g_2 \quad &- \quad (p_1 y_1 + p_2 y_2) - p_c(y_2 + y_1) + \frac{(p_1 + p_2)}{2}y_n \\
&+ \quad \pi^- y^- - \pi^+ y^+ + \frac{p_c}{2}\frac{|A_1 \times A_2|}{|S \times N|} = 0 \\
&\text{where } g_1 = \frac{S_1 \cdot N}{|S \times N|}, \quad g_2 = \frac{S_2 \cdot N}{|S \times N|}
\end{aligned} \tag{2.16}$$

Since π^+ is defined on $(j + 1)$ surface, it should be equal to π^- from the conservation cell defined between $(j + 1)$ and $(j + 2)$ surfaces if the conservation laws are to be satisfied, resulting in the reduced N momentum equation.

First , Equation (2.16) is rearranged into more convenient forms, by adding and sub-

tracting Equation (2.13).

$$mq_1g_1 \quad - \quad mq_2g_2 - (p_1y_1 + p_2y_2) - p_c(y_2 + y_1) + \frac{(p_1 + p_2)}{2}y_n$$
$$+ \quad p_c\frac{|A_1 \times A_2|}{|S \times N|}\frac{(y_2 + y_1)}{2} = -2\pi^-y^- \tag{2.17}$$

$$mq_1g_1 \quad - \quad mq_2g_2 + (p_1y_1 + p_2y_2) + p_c(y_2 + y_1) + \frac{(p_1 + p_2)}{2}y_n$$
$$+ \quad p_c\frac{|A_1 \times A_2|}{|S \times N|}\frac{(y_2 + y_1)}{2} = 2\pi^+y^+ \tag{2.18}$$

Then, by equating π^+ from (j) conservation cell to π^- from $(j + 1)$, the reduced N-momentum equation is obtained, which is refered as RN-momentum equation later on. The index (i, j) on π denotes the surface on which π is acting.

RN-momentum equation :

$$\pi^+_{i,j} = \pi^-_{i,j} \tag{2.19}$$

As mentioned in section 2.2.2, two variables are to be determined by S-momentum and N-momentum equations: the density $\rho_{i,j}$ and grid point position $n_{i,j}$. To constrain each variable, it is desirable to use the equation which is most sensitive to that variable, which contributes to the well-posedness of the problem. Computationally, this translates into a Jacobian matrix with strong diagonal terms. The RN-momentum equation is essentially the definition of stream-surfaces, that is, same pressure on both sides of that surface with no flux through it. It is most sensitive to the location of grid points, and mostly determines n_{ij}, while the S-momentum equation mostly determines the density $\rho_{i,j}$. However, reversing the assignment also works without any problem, because the sensitivities of these two equations are of the same order. This feature is used later in section 2.4.6 to eliminate redundancy of equations.

2.2.4 Upwinding in supersonic region

The discretized equations in previous section are well suited to the physics of subsonic flow. However, changes must be made to comply with the hyperbolic nature of supersonic flow. Because grid points are on the stream-surfaces, all characteristic lines align with the conservation cell. Therefore, the upwinding of (i) index to $(i - 1)$ makes the discretization

cell capture the wave-like physics of supersonic flow. Drela [17], Giles [19], and Youngren [57] showed that upwinding of either speeds or densities with proper switching in S-momentum and RN-momentum equations constitute a well behaving shock capturing method with conservative properties across a shock. In this thesis, the speed upwinding of Drela [17] is employed, which is given below.

$$
\begin{aligned}
\bar{q}_1 &= q_1 - \lambda_1(q_1 - q_0) \\
\bar{q}_2 &= q_2 - \lambda_1(q_2 - q_1) \\
&\text{where} \quad \lambda_2 = max(0, \frac{\bar{M}^2 - M_c^2}{\gamma \bar{M}^2}), \quad \bar{M}^2 = max(M_1^2, M_2^2)
\end{aligned}
\tag{2.20}
$$

In supersonic flow, q_1, q_2 of Equation (2.15), (2.19) are replaced with $\bar{q}_1, \bar{q}_2$. M_c is selected around 0.90, to maintain numerical stability.

2.3 Boundary layer equations and coupling

In this section, axisymmetric integral boundary layer equations are derived and discretized for the purpose of strong coupling of viscous flow to the inviscid flow, which is governed by the Euler equations. The instability of weak coupling methods has been well known and this approach is almost forgotten now with the rapid evolution of computing resources. However, resource requirements for Navier-Stokes solvers are still demanding, leaving a space for efficient Euler solvers with strong coupling like ISES [16].

2.3.1 Axisymmetric boundary layer equations

Axisymmetric boundary layer equations for non-conducting flows can be written as Equation (2.21), which is valid for small ratio of thickness to radius. Note that ξ, η are shear layer coordinates, while y denotes local radius. u, v are velocities in the direction of ξ, η , while u', v' represent turbulent fluctuation velocities.

$$
\frac{\partial(y\rho u)}{\partial \xi} + \frac{\partial(y\rho v)}{\partial \eta} = 0
\tag{2.21}
$$

$$
y\rho u \frac{\partial u}{\partial \xi} + y\rho v \frac{\partial u}{\partial \eta} = -y\frac{dP}{d\xi} + \frac{\partial}{\partial \eta}[y(\mu \frac{\partial u}{\partial \eta} - \rho \overline{u'v'})]
\tag{2.22}
$$

20

2.3.2 Integral boundary layer equations

Follwing procedures pioneered by von Karman, integral forms are derived as given below.

Momentum integral equation :

$$\frac{1}{\theta}\frac{d\theta}{d\xi} = \frac{1}{\theta}\frac{C_f}{2} - (\frac{\delta^*}{\theta} + 2 - M_e^2)\frac{1}{U_e}\frac{dU_e}{d\xi} - \frac{1}{y_e}\frac{dy_e}{d\xi} \qquad (2.23)$$

Shape parameter equation :

$$\frac{1}{H^*}\frac{dH^*}{d\xi} = \frac{2C_D}{\theta H^*} - \frac{1}{\theta}\frac{C_f}{2} - [2\frac{H^{**}}{H^*} - H + 1]\frac{1}{U_e}\frac{dU_e}{d\xi} \qquad (2.24)$$

Thicknesses and coefficients :

$$\delta^* = \int_0^\infty (1 - \frac{\rho u}{\rho_e U_e})\frac{y}{y_o}d\eta \ , \ \ \theta = \int_0^\infty (1 - \frac{u}{U_e})\frac{y\rho u}{y_o\rho_e U_e}d\eta \ , \ \ C_f = \frac{2}{\rho_e U_e^2}\tau_w \qquad (2.25)$$

$$\theta^* = \int_0^\infty [1 - (\frac{u}{U_e})^2]\frac{y\rho u}{y_o\rho_e U_e}d\eta \ , \ \ \delta^{**} = \int_0^\infty (1 - \frac{\rho}{\rho_e})\frac{yu}{y_o U_e}d\eta \qquad (2.26)$$

$$C_D = \frac{1}{\rho_e U_e^3}\int_0^\infty \frac{y}{y_e}\tau\frac{\partial u}{\partial y}dy \qquad (2.27)$$

Shape factors :

$$H = \frac{\delta^*}{\theta} \ , \ \ H^* = \frac{\theta^*}{\theta} \ , \ \ H^{**} = \frac{\delta^{**}}{\theta} \qquad (2.28)$$

Integral form of axisymmetric boundary layer equations are distinguished by a radius change term $\frac{1}{y_e}\frac{dy_e}{d\xi}$ in momentum equation, which represents streamline convergence(or divergence) due to radius changes of along the boundary layer. The thicknesses approach their two-dimensional definitions as ratio of thickness to edge radius gets closer to zero.

For closure and transition relations, proven two-dimensional models of Drela [17] are used. They are based on self-similar Falkner- Skan flow family, and curve fitting of turbulent-flow profiles, covering wide range of pressure gradient, Reynolds number, and Mach number. Transition is determined by the e^n envelope method, which is formulated by curve-fitting of Orr-Somerfeld solutions.

$$H_k = H_k(H, M_e) \ , \ \ H^* = H^*(H_k, M_e, Re_\theta) \ , \ \ H^{**} = H^{**}(H_k, M_e) \qquad (2.29)$$

$$C_f = C_f(H_k, M_e, Re_\theta) \ , \ \ C_D = C_D(H_k, M_e, Re_\theta, C_\tau) \qquad (2.30)$$

21

The most important parameter in closure relations is the kinematic shape factor H_k, which approaches its two-dimensional definition as ratio of boundary layer thickness to the radius of body gets small. In fact, a few boundary layer experiments used for the two dimensional closure were done on axisymmetric cylinders to take advantage of simple model geometry, justifying usage of 2D relations in this research. Furthermore, the axisymmetric boundary layer has no self similarity for decelerating flows, essentially preventing axisymmetric closure relations. Detail of closure and transition relations is omitted here with a full credit to Drela [17].

Equation (2.23),(2.24) are discretized by using logarithmic differencing. Along with these two, amplification factor equation is discretized to determine the transition point in laminar portion of boundary layer, while the lag equation is employed in turbulent portion to reflect upstream history. Detail of those equations are also described in Drela [17].

Momentum equation :

$$\frac{\ln{(\theta_2/\theta_1)}}{\ln{(\xi_2/\xi_1)}} - \frac{\xi_a}{\theta_a}\frac{C_f}{2} + (H_a + 2 - Me_a^2)\frac{\ln{(Ue_2/Ue_1)}}{\ln{(\xi_2/\xi_1)}} - \frac{\ln{(y_{e2}/y_{e1})}}{\ln{(\xi_2/\xi_1)}} = 0 \qquad (2.31)$$

Shape parameter equation :

$$\frac{\ln{(H_2^*/H_1^*)}}{\ln{(\xi_2/\xi_1)}} + \frac{\xi_a}{\theta_a}(\frac{C_f}{2} - \frac{2C_D}{H^*}) + (\frac{2H^{**}}{H_a^*} + 1 - H_a)\frac{\ln{(Ue_2/Ue_1)}}{\ln{(\xi_2/\xi_1)}} = 0 \qquad (2.32)$$

2.3.3 Coupling with inviscid flow

Viscous flow in boundary layer continues to lose the momentum to viscous friction as the flow passes along the surface. The slowed flow also gains in thickness to meet mass conservation, and thus the inviscid flow part feels the effect of boundary layer in the form of displacement of actual surface geometry by the amount δ^*. The stream-surface grid system facilitates a simple coupling of boundary layer and inviscid flow.

On body surfaces :

$$n_j = \bar{n}_j + \delta_j^* \qquad (2.33)$$

where $\bar{n}$ is the position of the surface.

On wake surfaces :

$$n_j - n_{j-1} = \delta_j^* + \delta_{j-1}^* \qquad (2.34)$$

2.4 Boundary conditions

To make the system of equations complete, a well-posed set of boundary conditions for densities and stream-surfaces should be applied on all flow boundaries ; inflow, outflow, body surface, symmetric axis, and the outermost streamsurface. The content of this section is the extension of three previous works. Potential boundary conditions for stream-surfaces are credited to Drela [17], while the well-posed set of boundary conditions for density, mass flow, and stagnation enthalpy stems from Giles [19]. The treatment of the redundant equation at the trailing edge originates from Drela [14].

2.4.1 Body surface

A solid body surface becomes a stream-surface itself in inviscid flow simulation, while viscous flow requires boundary layer coupling shown in Equation (2.33) (see Figure 2-5).

Solid surface :

$$\delta n_j = 0 \tag{2.35}$$

2.4.2 Flow passage interface

Passage interface surfaces are still stream-surfaces and there should be no gap and no pressure jump between them. When there is a boundary layer, the gap equals to the displacement thickness of wake, as given in Equation (2.33). Note the difference of 1 in j indices. Because stream-surface divides into two surfaces at the leading edge stagnation point, one more stream-surface is introduced at each flow passage interface.

Passage interface :

$$
\begin{aligned}
\delta n_j - \delta n_{j-1} &= 0 \\
\pi_j^- - \pi_{j-1}^+ &= 0
\end{aligned}
\tag{2.36}
$$

2.4.3 Potential boundary condition

At a far distance, the flow feels the body as a small disturbance. It was modeled as a combination of source, vortex, and doublet by Drela [17]. By analogy, vortex ring and

Pressure (potential)

**Inflow
Slope
(potential)**

Boundary layer Coupling

**Outflow
Slope
(potential)**

Solid Surface
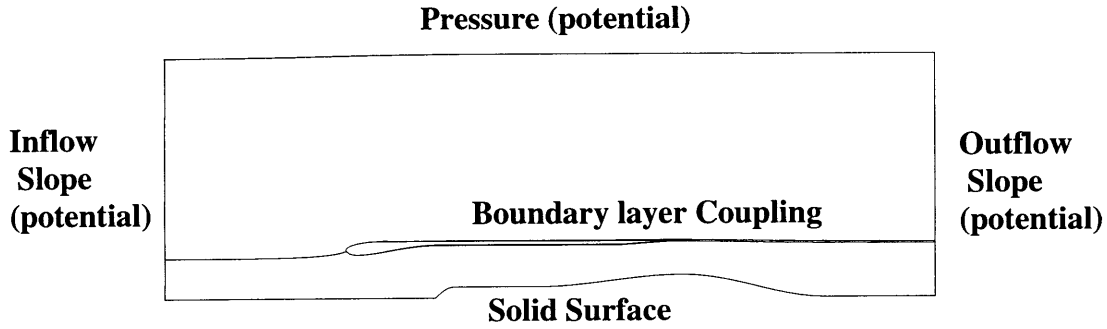
Figure 2-5: Boundary conditions on stream-surfaces

source ring formulations are derived for axisymmetric farfield boundary conditions. The doublet is excluded since it decays as $1/r^3$ compared to $1/r^2$ in two-dimensional flow. The source ring represents the mass defect which is closely related with drag of the body (refer Drela [17]). In the case of a powered engine, negative mass source means thrust. The vortex ring represents the suction of the flow into the engine and does not contribute to thrust or drag. The axial location of potentials is the moment center of the nacelle, while the radius of nacelle camberline is used as y_o.

$$\phi = \phi_s(Source) + \phi_v(Vortex) \tag{2.37}$$

The following expressions are perturbation velocities from source and vortex rings centered at $(0, y_o)$ (Figure 2-6). Compressibility is accounted in the form of Prandtl-Glauert transformation, whose effect is to elongate the distance x and amplify the u component of velocity.

Source ring :

$$
\begin{aligned}
u_s &= \frac{\Sigma x y_o}{\pi} \frac{1}{\sqrt{x^2 + (y_o + y)^2}} \frac{1}{[x^2 + (y_o - y)^2]} E \\
v_s &= \frac{\Sigma y_o}{\pi y} \frac{1}{\sqrt{x^2 + (y_o + y)^2}} \{K + \frac{(y^2 - y_o^2 - x^2)}{x^2 + (y_o - y)^2} E\}
\end{aligned} \tag{2.38}
$$

24
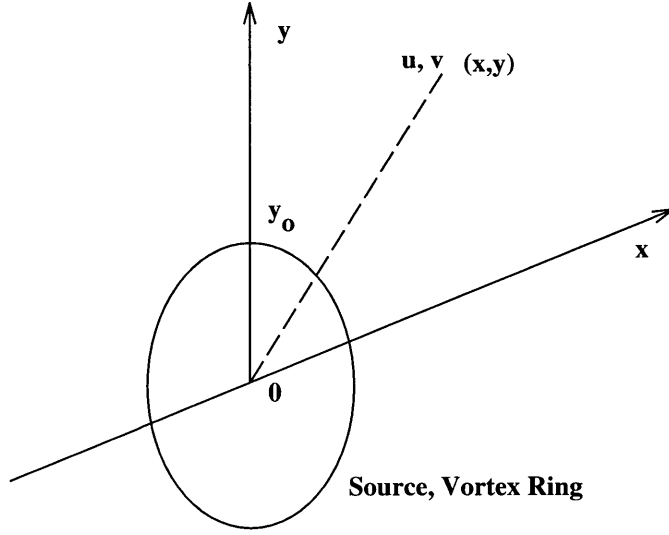
Figure 2-6: Source and vortex rings

Vortex ring :

$$
\begin{aligned}
u_v &= \frac{\Gamma}{2\pi} \frac{1}{\sqrt{x^2 + (y_o + y)^2}} \{ K - [1 + \frac{2(y - y_o)y_o}{x^2 + (y_o - y)^2}]E \} \\
v_v &= \frac{-\Gamma x}{2\pi y} \frac{1}{\sqrt{x^2 + (y_o + y)^2}} \{ K - [1 + \frac{2yy_o}{x^2 + (y_o - y)^2}]E \}
\end{aligned}
\tag{2.39}
$$

where complete elliptic integrals are

$$
\begin{aligned}
k^2 &= \frac{4yy_o}{x^2 + (y_o + y)^2} \\
E &= \int_0^{\frac{\pi}{2}} \sqrt{1 - k^2 \sin^2 \phi} \, d\phi \\
K &= \int_0^{\frac{\pi}{2}} \frac{1}{\sqrt{1 - k^2 \sin^2 \phi}} \, d\phi
\end{aligned}
\tag{2.40}
$$

Compressibility correction :

$$
\begin{aligned}
x_{comp} &= \frac{x}{\sqrt{1 - M^2}} \\
u_{comp} &= \frac{u_{incomp}}{\sqrt{1 - M^2}} \\
v_{comp} &= v_{incomp}
\end{aligned}
\tag{2.41}
$$

25

Since elliptic integral values are not found in exact explicit forms, series approximations are used (Gradshteyn and Pyzhik [20]). The order of series approximation is adjusted for each calculation to maintain accuracy (usually set at 10^{-5}). Note that u_{incomp} listed above means u is calculated from Equation (2.38),(2.39) with x_{comp} substituted into formulae instead of x. These perturbation velocities are used in two ways. First, they are used to specify the slope of stream-surface at inflow and outflow boundaries. Second, they are used to calculate the pressure on the outermost stream-surface of the computational domain, which is used as the boundary condition on that surface.

2.4.4 Potential strength

The source strength is determined from three contributions: mass defect due to boundary layer displacement thicknesses, stagnation pressure loss from shocks, and stagnation pressure loss or gain from the fan. In an actual calculation, the last two are done as the second term of left hand side of Equation (2.42), on the outflow boundary cells. NX is the i index of outflow boundary cells, while NY is the number of streamtubes. The first term is the contribution from the boundary layers, where y_e is the edge radius and NB is the number of boundary layers.

$$\Sigma = \frac{1}{y_o} \sum_{l=1}^{NB} (y_e \delta^*)_l^{exit} + \frac{1}{y_o} \sum_{j=1}^{NY} [\frac{1}{(\rho u)_{NX,j}} - \frac{1}{(\rho_\infty u_\infty)}] y_{aj} m_j \qquad (2.42)$$

where y_{aj} is the radius of j-th cell center and

$$(\rho u)_{NX,j} = (2h_t)^{\frac{1}{2}} [1 - (\frac{p_\infty}{p_t})_j^{\frac{\gamma-1}{\gamma}}]^{\frac{1}{2}} \frac{\gamma}{\gamma - 1} \frac{p_\infty}{h_t} (\frac{p_t}{p_\infty})_j^{\frac{\gamma-1}{\gamma}} \qquad (2.43)$$

On the other hand, the vortex strength needs a more approximate model for its determination. The role of the vortex ring is to increase or decrease mass flow through the nacelle, and thus, it is better determined by mass flow balance. But, unlike in two-dimensional flow, the stream function of a vortex ring is not available in explicit form and is calculated from numerical integration of velocity components given in Equation (2.39) (Küchemann [30]). The velocity components become singular near the vortex ring, blocking accurate integrations. As a practical detour, the stream function is integrated only to the surface of the nacelle, which is denoted as m_v in Equation (2.44). Also, the mass defect due to the

source potential is deducted in the mass flow balance consideration.

$$m_{nacelle} = \rho_\infty u_\infty (\Gamma m_v + \frac{1}{2} y_o{}^2 - \Sigma y_o) \qquad (2.44)$$

2.4.5 Stream-surfaces at inflow and outflow boundaries

The flow angle from perturbation velocities is specified as slope on each stream-surface. Note that u, v are summations of perturbation velocities from the source and vortex potentials. $I2$ is the i index for outflow boundary, with $NX = I2 - 1$ (Figure 2-5).

Inflow:

$$\frac{y_{2,j} - y_{1,j}}{x_{2,j} - x_{1,j}} = \frac{v}{U_\infty + u} \qquad (2.45)$$

Outflow:

$$\frac{y_{I2,j} - y_{NX,j}}{x_{I2,j} - x_{NX,j}} = \frac{v}{U_\infty + u} \qquad (2.46)$$

2.4.6 Flow variables

It has been shown by Giles [19] that specifying stagnation density, stagnation enthalpy, and mass flow rate at inflow boundary constitute a set of well-posed boundary conditions for an unchoked flow. He also showed that the mass flow of a choked flow should be determined by the flowfield with the back pressure specified at outflow boundary, which was shown to work for unchoked flow also. In engine flows, the engine core flow passage is virtually always choked, while the fan flow passage is designed to be unchoked. But, because the fan flow passage also has a possibility of being choked, all flow passages that flow between two body surfaces are better to be accompanied by the boundary conditions for the choked flow. The unchoked flow boundary conditions are appropriate for the outermost flow passage which has an unconfined free boundary and is never choked. But, it also has been observed that treating all flow passages with the choked flow boundary conditions works just fine.

In both cases, the stagnation enthalpy of each streamtube in the flow passage is equated to free stream value.

$$h_t = h_{t\infty} \qquad (2.47)$$

Choked flow passage

The densities of inflow boundary $\rho_{1,j}$ are determined by the free stream stagnation density. According to Giles [19], they are determined by

$$(\rho_t)_{1,j} - (\rho_t)_{1,j-1} = 0 \qquad (2.48)$$

which came from an observation of Crocco's theorm. Equation (2.48) makes $(J-1)$ equations for J streamtubes, and thus, J densities. The gap is filled with a S-momentum equation shifted from $(2,j)$ cell. For a single duct problem like a Laval nozzle, this shifting continues to the outflow boundary cell, where back pressure is specified to fill the gap. Physically, this shifting represents the way the flow feels the back pressure outflow boundary condition.

Outflow boundary of single duct flow:

$$p_{NX,JT} = P_e \qquad (2.49)$$

where JT is j index of streamtube with shifted equation.

By analogy , the shifting for a multi-passage flow problem ends at the trailing edge of the body surface that lies on the top stream-surface of each flow passage (Figure 2-7). At the trailing edge, one RN-momentum equation becomes redundant because the trailing edge should have no pressure jump while the surface boundary condition of Equation (2.35) still holds. The redundant RN-moment equation is then used to fill the equation gap through the interchange of RN-momentum equations. As a result, the equation gap is filled with a RN-momentum equation, which is an analogy of prescribing back pressure of the single duct problem.

Mass flow is determined to satisfy the specified inflow stagnation density condition. By fixing the stagnation density of one streamtube in the flow passage, all streamtubes have the same stagnation density from Equation (2.48).

Equation for mass flow m_k:

$$(\rho_t)_{1,JT} = \rho_{t\infty} \qquad (2.50)$$

28

Unchoked flow

The mass flow of outermost passage is fixed, and the densities of the inflow boundary cells are determined from the stagnation density.

Equation for density :

$$(\rho_t)_{1,j} = \rho_{t\infty} \qquad (2.51)$$
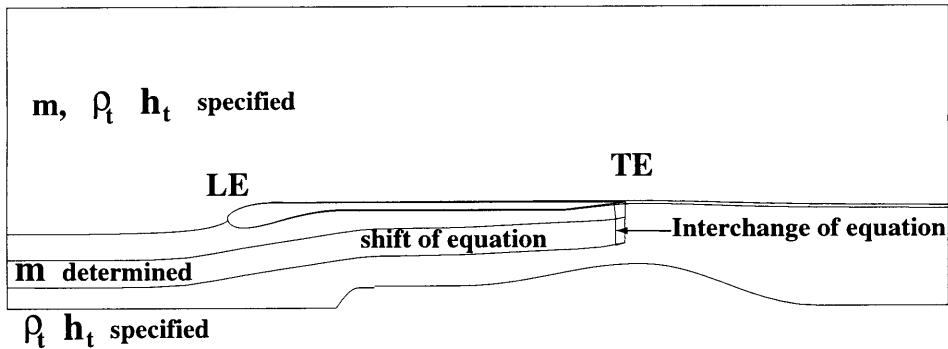
Figure 2-7: Boundary conditions on inflow boundary

2.5 Fan modeling and mass flow ratio (MFR)

The fan disk is modeled as an actuator disk with jumps in stagnation enthalpy, stagnation density, and pressure (Horlock [25]). A jump in swirl velocity is also possible at no extra cost, but is not employed here, because the swirl component of flow velocity is small compared to the meridional component in the fan flow passages of most engines. In fact, struts supporting a nacelle are designed to reduce swirl velocity after the fan disk, since the flow exiting with swirl velocity contains a wasted portion of kinetic energy. Before the fan disk, there is virtually no swirl component, unless the free stream has swirling velocity before it enters the nacelle. Like the fan flow passage, the engine core flow has little swirl component upon exiting the last turbine stage. Therefore, the engine core flow can be modeled as a series of actuator disks which have no swirl jumps, for the nacelle flow analysis/design purposes.

However, a jump in swirl velocity becomes a must for the simulation of the engine core flow where the swirl component is of the same order as the meridional component of flow velocity. The engine core flow is one of the least likely flow regimes that can be modeled by the steady axiymmetric Euler equations coupled with the integral boundary layer equations, due to the complex nature of the flow. But, the computing resource requirement for the numerical simulation of the unsteady engine core flow exceeds what current computer technologies can provide by far, even without any coupling with the fan flow passage. As a stopgap measure to this problem, the steady axisymmetric Euler equations and the actuator disk model have been used to find the 'average flow' solution (for example, Wu [56]), and it is expected to continue in the future.

The stagnation enthalpy jump is applied to the discretized form of the energy equation Equation (2.12), which is nothing more than an algebraic addition (Figure 2-8). Also, a stagnation density jump relation replaces the S-momentum equation, which constrains the density ρ_2.

Stagnation enthalpy jump across the fan :

$$h_{t\infty} + \Delta h_t = \frac{\gamma}{\gamma - 1}\frac{p_2}{\rho_2} + \frac{1}{2}q_2^2 \tag{2.52}$$

Stagnation density jump across the fan :

$$\rho_{t1} - \rho_{t2} = \Delta \rho_t \tag{2.53}$$

The strength of the fan is better left as a variable rather than be fixed, to provide some useful features, like matching mass flow ratio(MFR) of an experiment through strength adjustments. MFR is defined as the ratio of the actual mass flow into the nacelle to the free stream mass flow that passes through the circular disk of radius r_{lip}(cowl lip radius, Figure 2-8). MFR less than 1.0 means that the stagnation streamline is attached on the inner nacelle surface called the 'diffuser', which occurs when the engine runs slower than the design speed. Sometimes, the accelerated flow which turns around the cowl lip becomes supersonic, accompanied by shocks and flow separations on the cowl surface. On the other hand, MFR greater than 1.0 indicates the stagnation point settled on the outer nacelle surface called the 'cowl', and typically occurs during take-offs. Like the low MFR case, the

30

turning flow can develop shocks and flow separations on the diffuser surface, which can lead to the engine stall.

$$MFR = (r_m/r_{lip})^2$$

ρ_t
h_t

$\rho_t + \Delta\rho_t$
$h_t + \Delta h_t$

r_m

r_{lip}
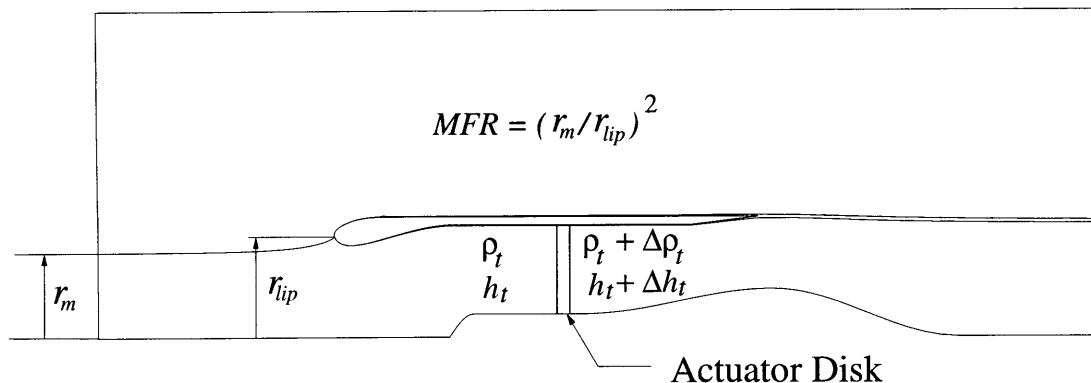
Actuator Disk

Figure 2-8: Actuator disk modeling of a fan

The mass flow ratio is without any doubt the most important parameter of nacelle operations, which is clearly seen in the results of this thesis. While the jump in stagnation enthalpy is changed as a variable, the jump in stagnation density can be related to that enthalpy jump through efficiency or loss considerations.

Equation for fan strength Δh_t :

$$m_k = m_{MFR} \qquad\qquad (2.54)$$

Finding the Jacobian components of Equation (2.54) requires some tricky steps, because there is no direct relation between mass flow ratio and other flow variables and geometry variables. Also, Equation (2.54) introduces a redundancy of equations, that is, it degenerates the independency of variables, which in turn, tends to slow the overall performance of the Newton method. This is similar to the introduction of a Lagrange multiplier for a constraint equation. Although it is clear that there is a disadvantage, the significance of MFR outweighs all the concerns.

The first step of the sensitivity calculation comes from the observation that any link between mass flow and other variables should come from the downstream of the fan, where the energy addition of a fan is applied. Pressure of a cell is one flow variable on which

31

mass flow rate m_k has a big influence. To reduce any adverse interaction with the rest of flow, a cell on outflow boundary is selected. Second, the sensitivity of pressure to mass flow variation in that cell is calculated in the usual manner, by perturbing a single variable and fixing others during FDM calculation. Finally, the chain rule for an analytic function is applied to find the sensitivities, which is shown for density ρ in Equation (2.55). All the other sensitivities follow similar procedures.

$$\frac{\partial m_k}{\partial \rho} = \frac{1}{\frac{\partial p}{\partial m_k}} \frac{\partial p}{\partial \rho} \qquad (2.55)$$

Before closing this section, effects of a fan on boundary layers should be mentioned. As a boundary layer passes, it experiences unsteady three dimensional forcing. It is most evident at the tip of the fan, with tip leakage flow and secondary vortices. This process is clearly beyond the scope of integral boundary layer formulation, and thus, no treatment or adjustment is currently done on boundary layers.

2.6 Newton solution procedure

A general non-linear system can be written as ;

$$R(Q) = 0 \quad (Q : \text{vector of variables}, \quad R : \text{vector of equations}) \qquad (2.56)$$

At iteration level m, the Newton solution procedure is

$$[\frac{\partial R}{\partial Q}]^m \delta Q^m = -R^m \qquad (2.57)$$

The structure of the resulting Jacobian matrix is described in Youngren [57] and Drela [17] in detail. For the calculation of the entries of the Jacobian matrix (called sensitivities), they used analytic differentiation together with the chain rule, which allows exact caculation of sensitivities at the cost of extensive bookeeping.

As an alternative approach, AMIS employs the finite difference method, to take advantage of its simple nature and the ability to handle complicated problems such as differentiation of elliptic integrals. Each variable is perturbed by finite amount from current iteration

level and the resulting residual change is then used to find sensitivity to that variable.

$$\frac{\partial R}{\partial q} = \frac{R(q + \Delta q) - R(q - \Delta q)}{2\Delta q} \quad \text{(other variables of } Q \text{ are fixed)} \qquad (2.58)$$

Typical perturbation is 1-0.1 % of current value and it has been observed that calculated sensitivities fall well within 0.5 % of error from exact values. For simple residuals like the slope boundary condition, the error becomes close to machine precision, while complicated residuals like the S-momentum equation show biggest errors. And also, the error can be reduced by orders of magnitudes through proper arrangement of terms in coding which affects round-off computation errors. For non-linear problems, the sensitivity itself is a linearization of the current solution and slight deviation from exact differentiation does not affect the converged solution, since this is determined by the residual functions alone. But, repeated calculation of residuals during differencing increases CPU time required for the generation of the Jacobian matrix. Actually, AMIS requires 20% of CPU time compared to roughly 10% for the ISES family.

Once the Jacobian matrix is composed, Equation (2.57) is processed with a block Gauss elimination solver, resulting in the correction vector δQ. When updating as shown in Equation (2.59), limit on the magnitude of correction is required during the first 2-3 iterations to stabilize initial transients, which is typically done by limiting the density correction to 20-30 % of the current value. The detailed block structure and inverting procedure of the Jacobian matrix is well discussed by Youngren [57] and Drela [17].

$$Q^{m+1} = Q^m + \delta Q^m \qquad (2.59)$$

2.7 Global variables and local variables

For an efficient matrix inversion process, it is necessary to group variables based on the direct influence of each variable, which results in a well structured Jacobian matrix. The influences of density ρ and stream-surface position n do not go beyond neighboring cells, and thus these are called local variables. On the other hand, all the other variables like the mass flow m_k and the source potential Γ can affect the whole flow field. Hence, these are called global variables.

All global variables were already discussed earlier, except the leading edge movement

33

S_{LE}, which moves on the surface. All the other grid points on the nacelle surface also move together like an accordion to maintain proper grid resolution around the leading edge. To control S_{LE}, pressure matching at the leading edge stagnation point is imposed as a leading edge Kutta condition. Note that there is an increase by 1 in j index across the interface.

$$\pi^+_{ILE,j-1} = \pi^-_{ILE,j} \tag{2.60}$$

2.8 Grid generation

Stream-surface based Newton solvers need a good starting solution for a reliable convergence. A converged solution makes a perfect starting point to other operating conditions or for re-designs. When the solver starts from scratch, care must be taken in the generation of initial grids, to which the solver reacts strongly. It is desirable to have stream-surface grids as a starting solution, although carefully constructed algebraic grids or elliptic grids may work sometimes. The approach of Wigton [55] was applied to two-dimensional Newton solver by Drela [14]. It is based on elliptic grid generation in the flow passage encompassed by stagnation streamlines which are integrated using a panel solution. In this thesis, it is extended to the axisymmetric problem, using the velocity formulations [Equation (2.38),(2.39)] of source ring and vortex ring along with the axisymmetric panel formulations by Küchemann [30] and Hess [24].

The potential solution part of the grid generator is a potential based axiymmetric panel solver with source and doublet distributions, and with doublet wake panels trailing the body (Youngren *et al.* [58]). Elliptic integral values are generated for a wide range of parameters and then stored for spline interpolations, which takes 2/3 less time than calculating by series approximation every time. Since the panel method is a mature concept with numerous publications, detail formulations are not covered here, with credits to Moran [35], Youngren *et al.* [58], and Sugioka [47].

Once the potential solution is found, the streamfunction is integrated numerically, which in turn is interpolated to generate streamlines. Finally, algebraic grids are generated on streamlines to desired grid resolution. The numerical integration procedure has some difficulty in very close vicinity of panel surfaces (usually less than 10 % of panel length) or close to the axis due to the singular behaviour of velocity components and the break-down of the

34

series approximation. Figure 2-9 shows algebraic grids generated on stream-surfaces, along with irregularities near the axis. These are mainly from the singular velocity behaviour near surfaces. This is left to be improved in the future through proper selection of data points of interpolation. Fortunately, the small mass flow in streamtubes near the axis reduces the influence of those irregularities on other cells, and no related difficulty has been observed in converging solutions from scratch using such initial grids.
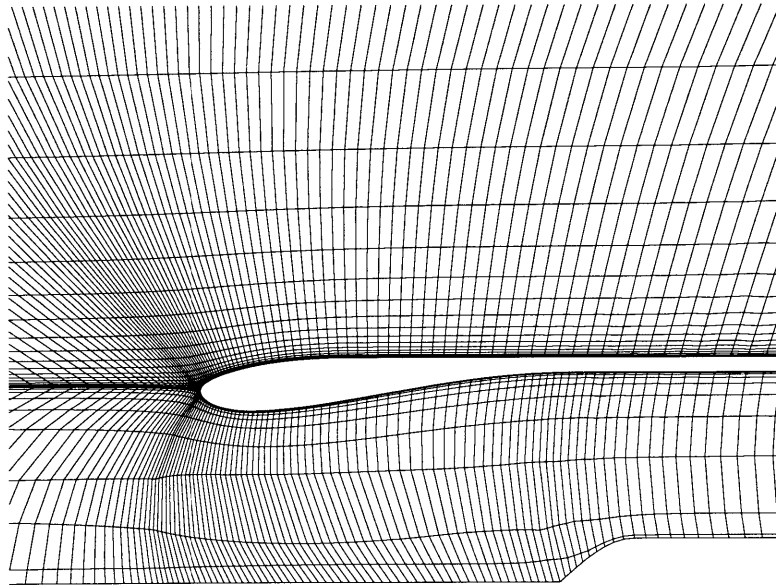
Figure 2-9: Stream-surface grids generated by the grid generator

Also, because the leading edge stagnation point floats along the surface, elliptic stream-surface grid smoothing is required after a Newton cycle to maintain proper grids during intial 3-4 iterations. A typical grid generation takes about 18 seconds on a SGI Indigo-I RS4000, which is slightly higher than one Newton iteration cycle. The post-cycle elliptic smoothing takes less than a second, though it retards the quadratic convergence of the Newton system.

2.9 Modal inverse design

The design method incorporated in this thesis is the adaptation of work by Drela [15], which has been in use in the industry since then. It can be applied to a portion of a surface or

camberline to maintain the thickness, either with boundary layer coupling or without. The underlying source of these versatile capabilities is the stream-surface grid system on which the solver is built. The surface movement in normal direction is represented as a sum of amplitudes of each design mode, which are shown in Figure 2-10 for 7 modified-sinusoid shapes.

$$\delta n_i = \sum_{l=1}^{L} \delta \tilde{n}_l g_l(s_i) \tag{2.61}$$

where L is number of geometric modes and $g_l(s_i)$ is the mode shape with amplitude $\delta \tilde{n}_l$. The numer of design modes and their shapes can be changed virtually without limit, as long as design modes are linearly independent.
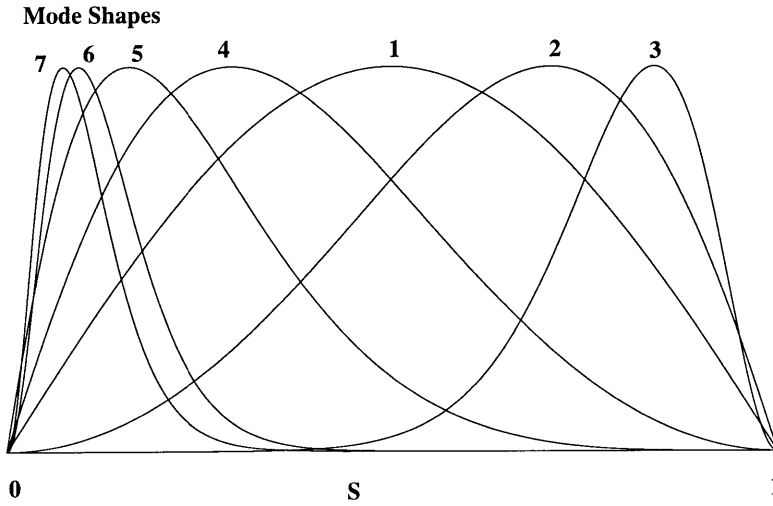
Mode Shapes

Figure 2-10: Design mode shapes

For each design mode, a global variable is assigned for its amplitude, which is determined by minimization of the difference between specified and calculated pressure, given as

$$I = \frac{1}{2} \sum_i [p_i(s_i) - p_{spec}(s_i)]^2 \tag{2.62}$$

The surface boundary condition also should be changed upon application of design modes,

$$\delta n_{i,j} = \delta(\delta_{i,j}^*) + \sum_{l=1}^{L} \delta \tilde{n}_l g_l(s_i) \tag{2.63}$$

given in linearized form. For the inviscid problem, the boundary layer term $\delta(\delta_{i,j}^*)$ is omit-

ted.

Chapter 3

Linearized three-dimensional flow theory

When an axisymmetric nacelle has an angle of attack, the flow becomes three-dimensional. If the angle of attack is small enough, the resulting three-dimensional flow can be represented by a superposition of the axisymmetric flow and a small three-dimensional perturbation flow. This flow situation is referred as 'quasi-3D' throughout this thesis. Although it depends on the flow phenomena to be linearized, a perturbation less than 10% can be regarded as 'small' generally. In terms of α, it translated into $\tan\alpha \leq 0.1$, or $\alpha \leq 5.7^o$.

Similar situations also can be found in the three-dimensional flows around a body whose geometry is close to axisymmetry. An engine nacelle for the podded engine installation like the Boeing 747 is designed around an axiymmetric geometry stipulated by the rotating nature of the engine. Upper cowl lip is extended forward and drooped down for stable air flow supply during high angle of attack flight, while more thickness is added on sides to prevent engine stalls induced by side wind. Some designs like the Boeing 737-300 are far from axisymmetry, but most nacelles are designed close to axisymmetry. The recent trend in the Boeing 777 and the ADP(Advanced Ducted Propulsor) of Pratt and Whitney is towards nearly axisymmetric nacelles.

As mentioned earlier in Chapter 1, existing three-dimensional flow solvers like NAS3D [51] and PARC3D [26] require about 80 hours of CPU on a CRAY-YMP for a Reynolds-averaged thin-layer Navier-Stokes flow simulation, while Euler solvers require 1-2 hours.

When a flow solution is expected to be quasi-3D, the linearization approach can be much more economical and effective. Since it is a linearization of the base axisymmetric flow solution, its computing resource requirements do not exceed what the axisymmetric Newton method requires by far, which are typically 4 minutes and 20 MB on a workstation. At this level, nacelle designers can try more concepts and configurations during initial design stages, while saving those expensive computations for a tough situation like the high angle of attack case.

Of course, there are some flow phenomena that can not be linearized properly due to their fundamental nonlinear natures like the shock formation from a subsonic flow, and the boundary layer separation from an attached flow. But, most nacelles are not designed to have such flows under cruise conditions where most quasi-3D flows are expected. In fact, most aerodynamic designs avoid shocks and separations if at all possible.

The base axisymmetry of the quasi-3D flow concept suggests the perturbations to be functions of the meridian angle ϕ measured counter-clockwise when viewed from the front of a nacelle. Fourier modes constitute a complete set and also offer the linear independency of modes, which is very useful in a linearization process. For a general vector of equations R, the linearization process for the first-order Fourier $\cos\phi$ mode perturbations becomes as follows.

$$
\begin{aligned}
R \quad & (Q + dQ\cos\phi) \\
= \quad & R(Q) + \cos\phi \, [\frac{\partial R}{\partial Q}] \, dQ + \text{Higher Order Terms} \\
= \quad & R(Q) + L\cos\phi
\end{aligned}
\tag{3.1}
$$

where Q is a vector of perturbation variables and L is the linearized residual vector. Once the base solution for $R(Q) = 0$ is known, the linearized solution is obtained by solving

$$
[\frac{\partial R}{\partial Q}] \, dQ = L
\tag{3.2}
$$

Due to the independency of the Fourier modes, the linearization process for each Fourier mode yields a separate equation similar to Equation (3.2).

However, the three-dimensional linearization requires non-zero $\frac{\partial}{\partial\phi}$ derivatives which in-

troduce couplings between the $\cos\phi$ modes and the $\sin\phi$ modes. The vector of equations T in Equation (3.3) represents the flux balances resulted from the differentiation of the perturbation modes with respect to the meridian angle ϕ, while R is the same vector of equations as the base axisymmetric flow problem.

$$
\begin{bmatrix} \frac{\partial R}{\partial Q_1}\cos\phi & \frac{\partial T}{\partial Q_2}\cos\phi \\ \frac{\partial T}{\partial Q_1}\sin\phi & \frac{\partial R}{\partial Q_2}\sin\phi \end{bmatrix} \begin{pmatrix} dQ_1 \\ dQ_2 \end{pmatrix} = \begin{pmatrix} L_1\cos\phi \\ L_2\sin\phi \end{pmatrix} \tag{3.3}
$$

where Q_1 is the vector of the $\cos\phi$ mode perturbations and Q_2 is the vector of the $\sin\phi$ mode perturbations.

Note that Q_1 can be a combination of the $\cos\phi$ modes and the $\sin\phi$ modes, as long as the linearized equations appear in $\cos\phi$. In that case, Q_2 is the 90° rotation of Q_1 in ϕ. The vector Q_2 is refered as 'horizontal set' henceforth, while Q_1 is refered as 'vertical set' to denote the orientation of the symmetry plane. The vertical set has a symmetry with respect to the meridional plane cut at $\phi = 0^o$ and $\phi = 180^o$. Also, note that the independency between the Fourier modes of different orders is still retained, allowing a separate linearization solution process for each order.

The couplings between the $\cos\phi$ modes and the $\sin\phi$ modes require double the size of the Jacobian matrix compared to the uncoupled problem, which also translates into quadruple the memory and CPU time requirements under the current matrix inversion process. However, when the base axisymmetric flow has no swirl velocity, these couplings can be avoided by a careful perturbation mode design which takes an advantage of the symmetry plane.

In this chapter, the quasi 3-D flow around an axisymmetric body with angle of attack α is linearized by the vertical set. The assumption of the non-swirling axisymmetric flow is reasonable, unless interested in the flow between the rotor/stator disk rows, since most engines are designed to have little swirl velocity after the last rotor/stator disk row.

In the following three sections, such symmetric geometric perturbation modes for the vertical set are presented, which are : eccentric mode, radius mode, and the angle mode. Each mode contributes to the momentum balance of a finite volume cell in three ways. First, net pressure forces on external surfaces change when surface areas change , second,

direction change of velocity vectors give perturbations in momentum flux balances, and third, change in the cross-sectional area normal to the velocity vector generates pressure and velocity perturbations. All other flow variables are also perturbed with proper modes in section 3.4- 3.7. These modes are followed by a proper set of boundary conditions for each mode in section 3.9, along with the exploration of the origin and elimination of potential instabilities in section 3.10. Then, a discussion on the rotation of the 'vertical set' into the 'horizontal set' follows in section 3.12, tailed by the extension to the higher-order Fourier modes, which closes this chapter.

All three-dimensional perturbations are denoted by 'd', while superscript A denotes an axisymmetric value. A variable which is a sum of an axisymmetric value and perturbation is marked with superscript $'$. Any other variable without these notations is an axisymmetric value and considered as a constant during linearization process. Also, 'first-order' refers to the order of a term in the perturbation variable, not the order of the Fourier mode.

3.1 Eccentric mode

This mode translates circular stream-surfaces along the vertical axis, while keeping them circular. Figure 3-1 shows the deformation of lateral surfaces of each streamtube when perturbation dy_j^{ec} is applied on (j) surface. Prescribing the eccentric mode at the farfield effectively specifies an angle of attack (Figure3-2) whose first-order effect is the tilting of streamtubes. Imposition of this mode on the nacelle surface can simulate the droop of the nacelle cowl lip.

The movement of the axis streamline is represented only by this mode ($dy_{j=2}^{ec}$), since the axis has zero radius, and hence can not be modeled by the radius mode whose description follows this section.

The first-order perturbations in momentum equations from the surface area changes and direction of velocity vectors due to the eccentric mode perturbation are found as follows. Notations of radii, vectors, and factors shown in Equation (2.4)- (2.8) are used again. Notations of y^{ec} are described in Figure 3-3.
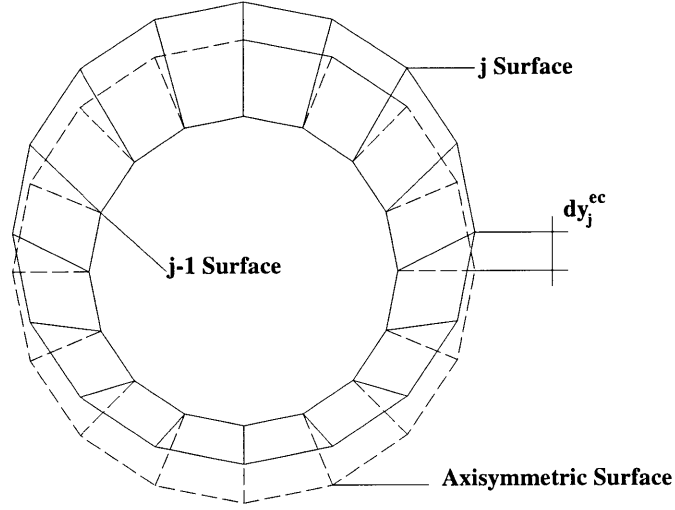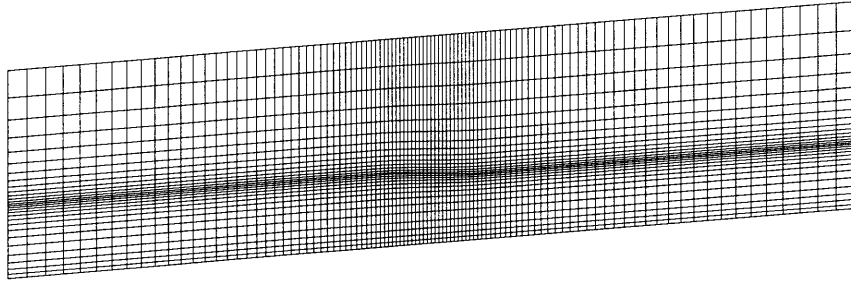
Figure 3-1: Eccentric mode shape

Figure 3-2: Grids with prescribed eccentric mode perturbations, $\alpha = 5.0^o$

Perturbations of x-momentum equation :

$$
\cos\phi \quad \{ \quad \frac{1}{2}p_1 y_1[(dy_{1+}^{ec} - dy_{1-}^{ec}) + (dy_{2+}^{ec} - dy_{2-}^{ec})] \; - \; \frac{1}{2}p_2 y_2[(dy_{2+}^{ec} - dy_{2-}^{ec}) + (dy_{3+}^{ec} - dy_{3-}^{ec})]
$$

$$
+ \quad \frac{1}{2}\pi^+ y^+(dy_{3+}^{ec} - dy_{1+}^{ec}) \; - \; \frac{1}{2}\pi^- y^-(dy_{3-}^{ec} - dy_{1-}^{ec})
$$

$$
+ \quad \frac{1}{4}p_a s_y[(dy_{1+}^{ec} + 2dy_{2+}^{ec} + dy_{3+}^{ec}) - (dy_{1-}^{ec} + 2dy_{2-}^{ec} + dy_{3-}^{ec})]
$$

$$
+ \quad \frac{1}{4}p_a y_n[(dy_{1+}^{ec} + dy_{1-}^{ec}) - (dy_{3+}^{ec} + dy_{3-}^{ec})]
$$

$$
+ \quad \frac{1}{2}(dy_{1+}^{ec} + dy_{1-}^{ec})\bar{q}_1 s_{x1} s_{y1}/s_1 \; + \; \frac{1}{2}(dy_{3+}^{ec} + dy_{3-}^{ec})\bar{q}_2 s_{x2} s_{y2}/s_2
$$

$$
- \quad \frac{1}{2}(dy_{2+}^{ec} + dy_{2-}^{ec})(\bar{q}_1 s_{x1} s_{y1}/s_1 + \bar{q}_2 s_{x2} s_{y2}/s_2) \quad \}
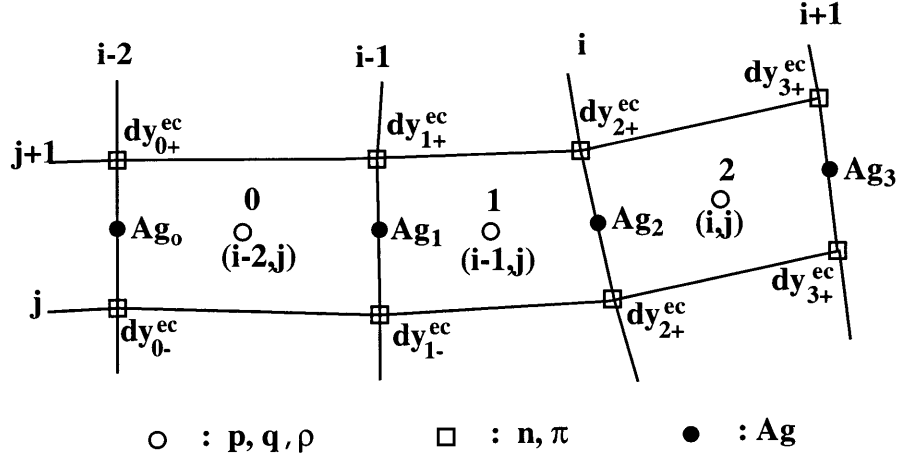$$

42

Figure 3-3: Notations of mode variables

where $\quad p_a = \dfrac{1}{2}(p_1 + p_2)$ $\qquad\qquad$ (3.4)

Perturbations of y-momentum equation :

$$\frac{\cos\phi}{2} \quad m\{ \quad (dy_{2+}^{ec} + dy_{2-}^{ec})(\bar{q}_1 s_{x1} s_{x1}/s_1 + \bar{q}_2 s_{x2} s_{x2}/s_2)$$
$$- \quad (dy_{1+}^{ec} + dy_{1-}^{ec})\bar{q}_1 s_{x1} s_{x1}/s_1 \quad - \quad (dy_{3+}^{ec} + dy_{3-}^{ec})\bar{q}_2 s_{x2} s_{x2}/s_2 \ \} \qquad (3.5)$$

The meridian angle ϕ is defined in counter-clockwise direction seen from front of nacelle, that is, 0° for upper lip and 180° for lower lip. Note that ϕ-momentum equation itself is in the first-order of perturbation variables, because axisymmetric equations do not consider the angular momentum equation.

Perturbations of ϕ-momentum equation :

$$\frac{\sin\phi}{2} \quad m[\quad (dy_{1+}^{ec} + dy_{1-}^{ec})\bar{q}_1/s_1 \quad + \quad (dy_{3+}^{ec} + dy_{3-}^{ec})\bar{q}_2/s_2$$
$$- \quad (dy_{2+}^{ec} + dy_{2-}^{ec})(\bar{q}_1/s_1 + \bar{q}_2/s_2) \ ] \qquad (3.6)$$

Normal area change on surface 1 :

$$dA_{n1} = \frac{1}{2} y_1 s_{x1}\{ \quad [(dy_{2+}^{ec} - dy_{2-}^{ec}) - (dy_{2+}^{ec} + dy_{2-}^{ec})(a_{x1} s_{x1} + a_{y1} s_{y1})/s_1]$$
$$+ \quad [(dy_{1+}^{ec} - dy_{1-}^{ec}) + (dy_{1+}^{ec} + dy_{1-}^{ec})(a_{x1} s_{x1} + a_{y1} s_{y1})/s_1] \ \}\cos\phi \quad (3.7)$$

Normal area change on 2 surface is given similarly , by changing indices of Equation (3.7) from (1,2) to (2,3). Because the area change follows the $cos\phi$ mode, it is clear that any pressure and velocity magnitude perturbation from the normal area change will follow the $cos\phi$ mode too. Following this, sensitivities of S-momentum and RN-momentum equations from pressure perturbations are calculated using the resultant perturbation of Equation (2.15) and (2.19), obtained by perturbing the normal area with finite amount of dy^{ec}. Also, there is a pressure perturbation term in ϕ-momentum equation , which comes from the differentiation of the pressure perturbation in the ϕ direction. Since pressure perturbation varies as $\cos\phi$, its contribution will be in $\sin\phi$, in line with other terms of Equation (3.6).

Pressure perturbation in ϕ-equation :

$$\frac{\partial(dp_a \cos\phi)}{\partial\phi} = -dp_a \sin\phi \qquad (3.8)$$

3.2 Radius mode

In this mode, the stream surface moves along the normal direction from the stream-surface while keeping the side surfaces of each stream tube undeformed. Figure 3-4 shows the dn_j perturbation on the (j) surface. The stream-surface remains circular to first-order. Applied on the nacelle surface, the radius mode can represent a perturbation of nacelle geometry.

The radius mode is relatively simple to implement, since all the sensitivities with respect to this mode are the same as the axisymmetric problem, which are already generated from FDM perturbations of Equation (2.15), (2.19). Of course, the ϕ-momentum equation has a pressure perturbation in the same form as Equation (3.8).

$$n'_{i,j} = n^A_{i,j} + dn_{i,j}\cos\phi \qquad (3.9)$$

3.3 Angle mode

The angle mode describes the angular movement of each streamtube, defined as a chunk of fluid moving by the amount of $A_{g_{i,j}}$ defined at the mid-point of the cell grid line (Figure 3-3). Note in Figure 3-5 that the circular shape of the stream-surface is maintained. Defining A_g's on grid points was also considered, but was later dropped due to obvious difficulties in
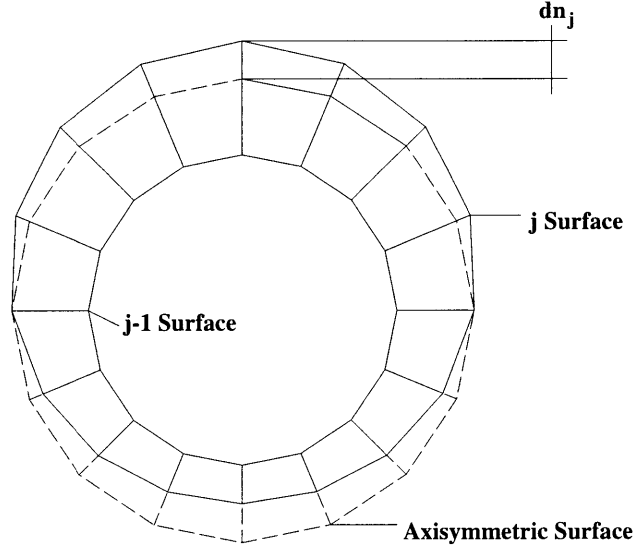
Figure 3-4: Radius mode shape

boundary conditions across passage interfaces. The superscript A denotes the angle location of the axisymmetric cell.

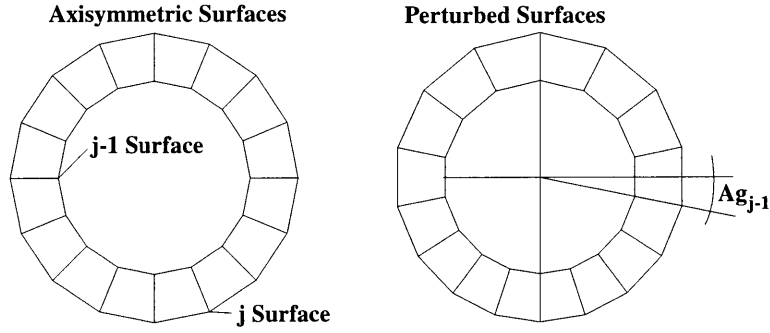$$\phi'_{i,j} = \phi^A + A_{g_{i,j}} \sin \phi^A \qquad (3.10)$$

Figure 3-5: Angle mode shape

The first-order perturbations in momentum equations from the surface area changes and direction of velocity vectors due to the eccentric mode perturbation are found as given below. Like the eccentric mode, sensitivities coming from pressure and velocity magnitude perturbations are calculated directly from finite differencing of Equation (2.15), (2.19) by perturbing the normal area with finite $A_{g_{i,j}} \sin \phi^A$.

Perturbation of x-momentum equation :

$$\frac{\cos \phi}{4} \quad \{ \quad A_{g1}[p_1 a_{y1} y_{a1} + \pi^+ b_y^+ y_{1-1,j+1} - \pi^- b_y^- y_{i-1,j} - p_a(y_n y_{a1} + s_y y_{d1})]$$

$$+ \quad A_{g2}[p_1 a_{y1} y_{a2} - p_2 a_{y2} y_{a2} + 2\pi^+ b_y^+ y_{i,j+1} - 2\pi^- b_y^- y_{i,j} - 2p_a s_y y_{d2}]$$

45

$$+ \quad A_{g3}[-p_2 a_{y2} y_{a3} + \pi^+ b_y^+ y_{i+1,j+1} - \pi^- b_y^- y_{i+1,j} - p_a(y_n y_{a3} + s_y y_{d3})] \quad \}$$

where $\quad y_{a1} = y_{i-1,j} + y_{i-1,j+1}$, $\quad y_{d1} = y_{i-1,j+1} - y_{i-1,j}$

$$y_{a2} = y_{i,j} + y_{i,j+1} , \qquad y_{d2} = y_{i,j+1} - y_{i,j}$$

$$y_{a3} = y_{i+1,j} + y_{i+1,j+1} , \quad y_{d3} = y_{i+1,j+1} - y_{i+1,j} \tag{3.11}$$

Perturbation of y-momentum equation :

$$\frac{\cos\phi}{4} \quad \{ \quad A_{g1}[-p_1 a_{x1} y_{a1} - \pi^+ b_x^+ y_{i-1,j+1} + \pi^- b_x^- y_{i-1,j} + p_a(x_n y_{a1} + s_x y_{d1})]$$

$$+ \quad A_{g2}[p_1 a_{x1} y_{a2} - p_2 a_{x2} y_{a2} - 2\pi^+ b_x^+ y_{i,j+1} + 2\pi^- b_x^- y_{i,j} + 2 p_a s_x y_{d2}]$$

$$+ \quad A_{g3}[p_2 a_{x2} y_{a3} - \pi^+ b_x^+ y_{i+1,j+1} + \pi^- b_x^- y_{i+1,j} + p_a(-x_n y_{a3} + s_x y_{d3})] \quad \} \tag{3.12}$$

Perturbation of ϕ-momentum equation :

$$\frac{\sin\phi}{2} \, m \, [\, A_{g3} y_{a3}(\bar{q}_1/s_1 + \bar{q}_2/s_2) - A_{g1}\bar{q}_1 y_{a1}/s_1 - A_{g3}\bar{q}_2 y_{a3}/s_2 \,] \tag{3.13}$$

Normal area change on surface 1 :

$$dA_{n1} = \frac{1}{4}(y_{a1} A_{g2} + y_{a1} A_{g2})(s_{x1} a_{y1} - s_{y1} a_{x1}) \cos\phi \tag{3.14}$$

Superposing the angle mode with the aforementioned radius mode results in a movement similar to the eccentric mode. In fact, it becomes the same mode to first-order in perturbation variables when the base axisymmetric finite volume cell is parallel to the axis, and on the application of following relations. Equation (3.15) describes the eccentric component of an angle mode, while the next two relations mean the eccentric components of the radius modes.

If the left hand side of Equation (3.15) is bigger than the right hand side, the difference is the pure angular stretching component as described in Figure (3-5).

$$A_{g_{i,j-1}}(y_{i,j-1} + y_{i,j}) = -(dy^{ec}{}_{i,j-1} + dy^{ec}{}_{i,j}) \tag{3.15}$$

$$dy_{i,j-1} = dy^{ec}{}_{i,j-1} \tag{3.16}$$

$$dy_{i,j} = dy^{ec}{}_{i,j} \tag{3.17}$$

This means that only two of the three geometric modes are necessary to model the

geometry perturbation properly. Thus, the angle mode and eccentric mode are used in cells adjoining the axis, while angle mode and radius mode are used in other cells, in which prescribed eccentric modes give non-zero residual terms. Figure 3-6 shows the superposition of the angle mode in (j-1) streamtube and the radius mode on (j) streamsurface, which is equivalent to the eccentric mode on (j) streamsurface, to first-order in perturbation variables. That is, outer cell surface areas, cell center movements, and cross-sectional cell areas are matched to first-order.
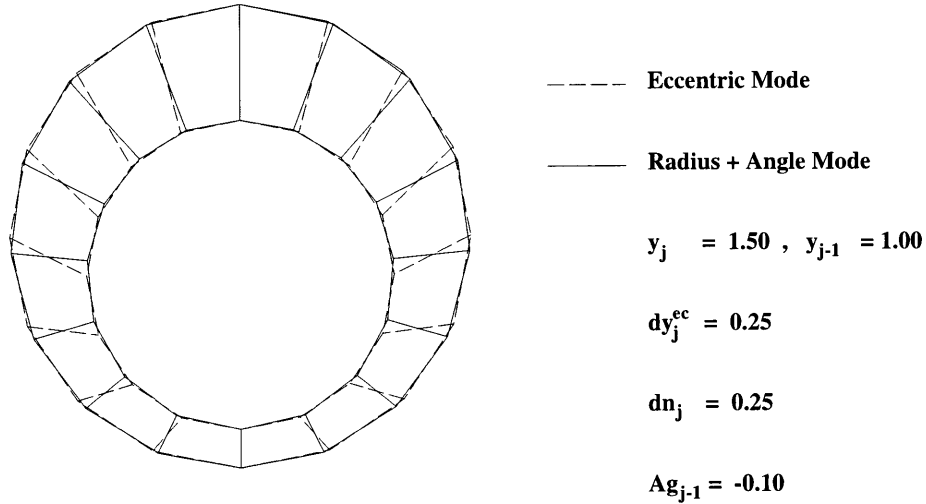

$----$ **Eccentric Mode**

$-----$ **Radius + Angle Mode**

$y_j = 1.50$, $y_{j-1} = 1.00$

$dy_j^{ec} = 0.25$

$dn_j = 0.25$

$Ag_{j-1} = -0.10$

Figure 3-6: Equivalent superposition of modes

3.4 Density mode

The density of each cell is perturbed by $\cos\phi$, and is constrained primarily by the perturbed S-momentum equation. In Equation (3.18), the superscript A denotes the density value of base axisymmetric flow.

$$\rho'_{i,j} = \rho^A_{i,j} + d\rho_{i,j}\cos\phi \tag{3.18}$$

3.5 Linearization of global variables

Among the global variables of the base axisymmetric flow, only the mass flow m_k and leading edge variable S_{LE} are linearized, while others are fixed. Effects of perturbations in the farfield potential strengths Γ, Σ are of the same order as the round-off errors of single precision, and thus are safely ignored. The fan strength is fixed for simplicity. A possible extension would allow for some variation of the strength distribution along ϕ.

47

The mass flow follows the $\cos\phi$ mode as

$$\dot{m}'_k = \dot{m}^A_k + d\dot{m}_k \cos\phi \qquad (3.19)$$

As in the base axisymmetric flow, stagnation density conditions control the magnitude of mass flow perturbations.

The leading edge stagnation point position is also represented by the $\cos\phi$ mode and determined by the leading edge Kutta condition.

$$S'_{LE} = S^A{}_{LE} + dS_{LE} \cos\phi \qquad (3.20)$$

3.6 Linearization of S and RN-momentum equations

The linearization process uses a mixture of exact and finite differenced derivatives. In the process, a careful grouping of terms by their order of magnitudes may be needed to reduce round-off errors. It becomes a must when the equation has addition or subtraction of terms with widely varying magnitudes, which is the case in the linearized equations. It has been observed that sensitivities can change as much as 4% upon different regrouping. As a detour to that problem, some linearization approaches are adopting double precision at the cost of more than doubling memory requirements. The CPU time might also be doubled on some processors.

The perturbations of the x-momentum and y-momentum equations due to surface area and velocity direction changes are described to first-order, and therefore, their coefficients of perturbation mode variables are the necessary mode sensitivities. The contributions from the normal area changes are calculated using FDM. For an example, sensitivity of the S-momentum equation with respect to A_{g1} is obtained as

$$
\begin{aligned}
\frac{\partial[Eq(2.15)]}{\partial A_{g1}} =& \\
\frac{\cos\phi}{4|S \times N|} &\quad \{ \quad s_x[p_1 a_{y1} y_{a1} + \pi^+ b_y^+ y_{1-1,j+1} - \pi^- b_y^- y_{i-1,j} - p_a(y_n y_{a1} + s_y y_{d1})] \\
&+ \quad s_y[-p_1 a_{x1} y_{a1} - \pi^+ b_x^+ y_{1-1,j+1} + \pi^- b_x^- y_{i-1,j} + p_a(x_n y_{a1} + s_x y_{d1})]\} \\
&+ \quad (\frac{\partial[Eq(2.15)]}{\partial A_{g1}})^{(dp_i, dq_i)} \qquad (3.21)
\end{aligned}
$$

where the last term is obtained by numerically perturbing Equation (2.15) with finite normal area change of Equation(3.14), while fixing all the other variables. The superscript (dp_i, dq_i) means pressure and velocity magnitudes are perturbed by the area change. The second line is the coefficient of A_{g1} from Equation(3.11), followed by the coefficient of Equation(3.12) on the third line. The RN-momentum equation follows a similar linearization process, except the factors s_x, s_y of Equation(3.21) are replaced with x_n, y_n.

The complete linearized equation is obtained by the summation of the sensitivities from each perturbation mode. Once linearized, the S-momentum equations primarily determine the density perturbations, and the RN-momentum primarily determine the stream-surface perturbations, as in the base axisymmetric flow.

3.7 Linearization of boundary layer equations

Undoubtedly, this section is the weakest part of this chapter, because some flow physics are ignored. Although three-dimensional integral boundary layer equations and closure relations of Mughal [36] are readily available, δ^*, θ, and $\tilde{n}$ (in laminar flow, $C_\tau^{\frac{1}{2}}$ in turbulent flow) of axisymmetric boundary layer formulations are simply perturbed in $\cos\phi$ modes, as a stop-gap measure.

The first-order effect of the boundary layer ϕ-momentum equation is to redistribute the streamwise momentum defect in ϕ. Hence, the total profile drag of the nacelle is expected to be insensitive to small three-dimensional perturbations. This partially justifies omission of the boundary layer ϕ-momentum equation from the quasi-3D formulation.

3.8 Swirl velocity calculation

The presence of swirl velocity is a key part of the linearized three-dimensional flow modeling, since it endows lift and downwash. It is first-order in perturbation variables and does not contribute to pressure variations or and momentum flux balances other than in the ϕ-momentum equation.

Swirl velocity is defined positive in the direction of the meridian angle ϕ at the same point where the angle is defined, and varies as $\sin\phi$. From the definition of geometric modes, the swirl velocity is the sum of the angle mode and the $\sin\phi$ component of the eccentric mode , while the radius mode does not contribute at all. Swirl velocity w_2 at the point of

49

A_{g2} definition in Figure 3-3 is derived as below.

Swirl velocity :

$$w_2 = \frac{\sin\phi}{4} \quad [\quad \frac{q_2}{s_2}(A_{g3}y_{a3} - A_{g2}y_{a2}) + \frac{q_1}{s_1}(A_{g2}y_{a2} - A_{g1}y_{a1})$$
$$- \frac{q_2}{s_2}(y_{3+}^{ec} + y_{3-}^{ec} - y_{2+}^{ec} - y_{2-}^{ec}) - \frac{q_1}{s_1}(y_{2+}^{ec} + y_{2-}^{ec} - y_{1+}^{ec} - y_{1-}^{ec}) \quad] \quad (3.22)$$

3.9 Boundary conditions

In this section, a proper set of boundary conditions for each perturbation mode is presented. Boundary conditions for the stagnation density ρ_t , stagnation enthalpy h_t, and mass flow m_k are straightforward linearizations of the axisymmetric flow problem mentioned in section 2.4, and thus omitted here.

3.9.1 Boundary conditions for radius mode and eccentric mode

Boundary conditions for the radius mode are three-dimensional extensions of the slope conditions along with the solid surface boundary conditions. At the inflow boundary, the stream-surfaces are aligned with the velocity which is the sum of farfield potential velocity and free stream. Because stream-surface movement is modeled with a combination of eccentric mode and radius mode, this slope condition is applied to the combination of two modes at the inflow boundary.

Radius mode at inflow :

$$\frac{dy_{2,j} + y_{2,j}^{ec} - dy_{1,j} - y_{1,j}^{ec}}{x'_{2,j} - x'_{1,j}} = \frac{v + \alpha U_\infty}{U_\infty + u} \tag{3.23}$$

On the outflow, the flow is not aligned closely to the free stream anymore, because there is the downwash generated by the nacelle. The downwash is closely related to swirl velocity as described in section 3.8 and maintained at a constant value near the outflow boundary where there is virtually no pressure perturbation, and the axisymmetric pressure distribution is close to uniform. Therefore, slope at outflow boundary is simply extrapolated from the slope of the upstream grid interval.

50

Radius mode at outflow :

$$\frac{dy_{I2,j} + y^{ec}_{I2,j} - dy_{NX,j} - y^{ec}_{NX,j}}{x'_{I2,j} - x'_{NX,j}} = \frac{dy_{NX,j} + y^{ec}_{NX,j} - dy_{NX-1,j} - y^{ec}_{NX-1,j}}{x'_{NX,j} - x'_{NX-1,j}} \qquad (3.24)$$

On the solid axisymmetric surfaces, the boundary conditions for the radius mode becomes the same as the axisymmetric flow.

Solid axisymmetric surface :

$$dn_j = 0 \qquad (3.25)$$

In addition to Equation 3.25, the eccentric mode can be specified to represent a drooped surface. This specified eccentric mode contributes to the residual vector L of Equation (3.2).

Drooped axisymmetric surface:

$$dn_j = 0 \ , \ \ dy^{ec}{}_j = dy^{droop}{}_j \qquad (3.26)$$

3.9.2   Inflow boundary condition for angle mode

At the inflow boundary, the swirl velocity should be zero everywhere, because the free stream is assumed to be irrotational. The formulation for swirl velocity is presented in section 3.8.

Angle mode on Inflow :

$$w_{i=2} = 0 \qquad (3.27)$$

3.9.3   Constraint on angle mode

The angle mode is unconstrained by nature, since body surfaces can constrain only the radius mode and the eccentric mode. To constrain this, a new global variable is introduced for each streamtube, at the expense of memory and CPU time. Addition of each global variable usually costs an additional 5% of CPU time under the current matrix inversion process, which treats sensitivities of global variables as additional right hand side columns.

As mentioned earlier in section 3.3, the superposition of the angle mode and the radius mode generates the eccentric mode to first-order. Thus, the constraint should be applied only to the angular stretching component of the angle mode, otherwise, other modes will be constrained improperly, affecting the whole flowfield. After extensive trial and error, a

successful constraint came from an application of Equation (3.15) as

$$A_{g_{I2,j}}(y_{I2,j} + y_{I2,j+1}) + (dy_{I2,j} + dy_{I2,j+1}) + 2(dy^{ec}_{I2,j+1} - dy^{ec}_{I2,j+1}) =$$

$$- [A_{g_{1,j}}(y_{1,j} + y_{1,j+1}) + (dy_{1,j} + dy_{1,j+1}) + 2(dy^{ec}_{1,j} - dy^{ec}_{1,j+1})] \qquad (3.28)$$

In Equation (3.28), ($i = 1$) denotes the inflow boundary, while ($i = I2$) denotes the outflow boundary. The second term of each side represents the eccentric component of the radius mode, while the third term is the angular stretching from the prescribed eccentric modes. The negative sign on the right hand side constrains the stretching component of the angle mode, by necessitating a zero amplitude somewhere in the streamtube. Another benefit of Equation (3.28) is the increase in the accuracy of solution, by finding the solution near the base axisymmetric solution, at which all sensitivities are calculated.

3.10   Instability mode and damping

Since swirl velocity is first-order in perturbation variables, it does not contribute to the pressure calculation of a cell at all. This allows an inherent saw-tooth instability in the angle mode (Figure 3-7), and is accompanied by an instability in the radius mode to satisfy mass flow conservation in the streamtube.
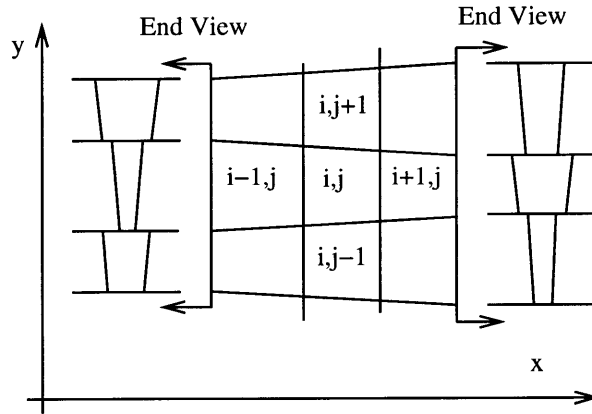

Figure 3-7: Instability of angle mode ($\phi = 0^o$ plane)

This can be suppressed to some extent near solid surface boundaries where the radius mode is fixed. But, in the stream-surface farther from the solid surface, the instability

52

becomes more dominant. One way to control this situation is by addition of a pressure correction to the RN-momentum or ϕ-momentum equations. But this also interferes with the constant angular stretching of streamtubes, which is expected in the downwash trailing the nacelle.

$$
\begin{aligned}
C_{np} &= C_n \gamma M^2 \frac{s_x(b'_{y+} - b'_{y-})}{|S \times N|} \\
\bar{d\pi}^+ &= d\pi^+ - \pi^+ C_{np} \\
\bar{d\pi}^- &= d\pi^- - \pi^- C_{np}
\end{aligned}
\tag{3.29}
$$

where, $\bar{d\pi}^-, \bar{d\pi}^+$ are corrected pressure perturbations and π^+, π^- are axisymmetric pressures. Typical C_n values are chosen between 0.01-0.06 depending on the problems. This is about 10-60% of the axisymmetric pressure correction given in Equation(2.14).

3.11 Linearized three-dimensional solution procedure

The angle mode represents the increase in the number of dimensions from 2 to 3, and is controled by the ϕ-momentum equation. Hence, the number of local variables per cell increases from 2 to 3, which doubles the Jacobian matrix in size. The memory requirement for the Jacobian matrix is proportional to the square of the number of local variables per cell. Each block in the Jacobian matrix shares the structure shown in Figure 3-8 to utilize the existing sensitivities of the axisymmetric flow problem, which are contained in a thick-lined rectangle in the upper-left corner.

Once the Jacobian matrix is constructed, it is inverted by the same matrix solver as the axisymmetric problem, resulting in the perturbation vector dQ. The linearized solution is obtained as the sum of the axisymmetric solution Q^A and the perturbation vector dQ.

$$
Q' = Q^A + dQ
\tag{3.30}
$$

3.12 Rotation of Fourier modes

The linear independency of Fourier modes allows a separate solution procedure for each mode. The set of perturbation modes mentioned in sections 3.1 - 3.5 is composed of the $\cos\phi$ radius mode, the $\sin\phi$ angle mode, the $\cos\phi$ density mode, and the $\cos\phi$ global

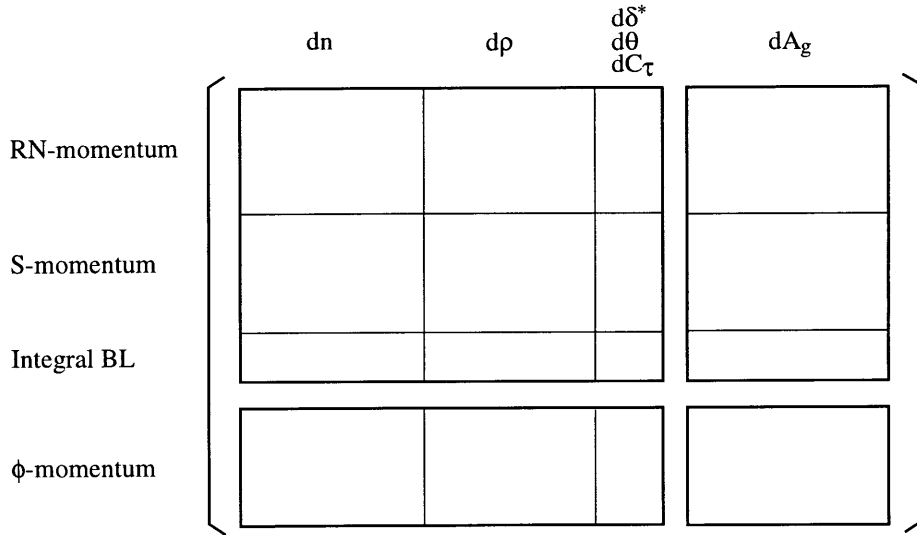|	dn	dp	$d\delta^*$ $d\theta$ dC_τ	dA_g
RN-momentum				
S-momentum				
Integral BL				
ϕ-momentum				

Figure 3-8: Block matrix structure

variable mode. This set represent symmetric perturbations with respect to the meridional plane cut at $\phi = 0^o$, $\phi = 180^o$, which is refered as 'vertical set'.

With a rotation by 90° in ϕ, the vertical set becomes a set of symmetric perturbations with respect to the meridional plane cut at $\phi = 90^o$, $\phi = -90^o$, which is refered as 'horizontal set'. The horizontal set is composed of the the $\sin \phi$ radius mode, the $-\cos \phi$ angle mode, the $\sin \phi$ density mode, and the $\sin \phi$ global variable mode. The specification of the side-slip angle β or the side-gust velocity has the same effect as the angle of attack α in the vertical set.

Since Fourier modes constitute a complete set in the description of a function, the superposition of the vetical sets and the horizontal sets to the desired order 'n' can simulate any quasi-3D flow to first-order of perturbation variables.

3.13 Extension to higher-order Fourier modes

The first-order Fourier perturbation modes described in previous sections are designed to model 'quasi-3D' flow around an axisymmetric body whose base axisymmetric flow has no swirl velocity.

The three-dimensional perturabtion of the axisymmetric body surface other than the eccentric translation can be represented by the superposition of higher-order radius modes

which are shown in Figure 3-9. Note that the eccentric mode is actually a superposition of the first-order Fourier radius mode and the angle mode. The eccentric mode is introduced to facilitate the application of the angle of attack condition and to model the movement of the axis streamline. Only the solutions for the first-order Fourier perturbation modes are affected by the angle of attack condition whose first-order effect is tilting streamtubes by the amount of the angle. Therefore, non-zero residuals for a higher-order linearization process come from the non-axisymmetric surface geometry only.

Figure 3-10 describes the higher-order Fourier angle modes. The linearized flux terms in Equation (3.5) - (3.13) which come from the differentiation with respect to ϕ are multiplied by 'n'. Also, the density mode and all the global variable modes follow the same order Fourier modes to complete the liearization process.
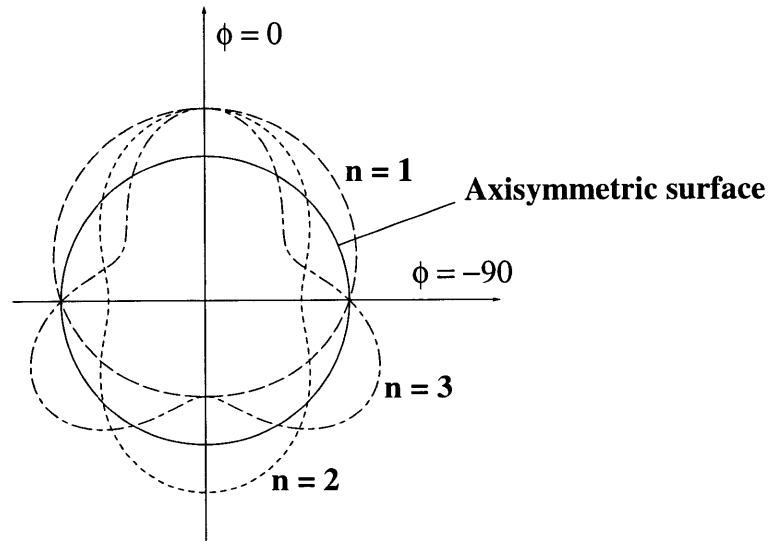
Figure 3-9: Higher-order Fourier radius modes

All boundary conditions for the first-order Fourier perturbation modes, which are covered in section 3.9, also apply to the higher-order Fourier perturbation problems, except the stream-surface boundary conditions which are found as follows. Note that y^{ec} should be removed from the boundary conditions of the first-order Fourier perturbation modes in order to be extended to the higher-order Fourier modes properly.

Radius mode at inflow :

$$\frac{dy_{2,j} - dy_{1,j}}{x'_{2,j} - x'_{1,j}} = 0 \tag{3.31}$$
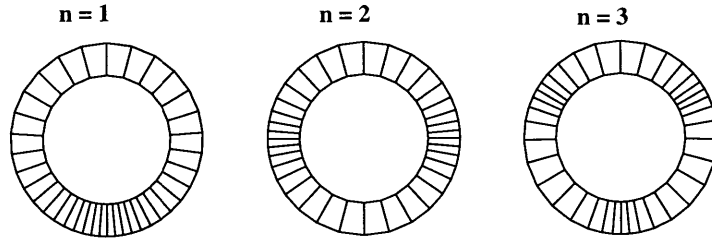
n = 1   n = 2   n = 3

Figure 3-10: Higher-order Fourier angle modes

Radius mode at outflow :

$$\frac{dy_{I2,j} - dy_{NX,j}}{x'_{I2,j} - x'_{NX,j}} = \frac{dy_{NX,j} - dy_{NX-1,j}}{x'_{NX,j} - x'_{NX-1,j}} \tag{3.32}$$

Solid surfaces :

$$dn_j = dn_j^{specified} \tag{3.33}$$

Chapter 4

Axisymmetric flow results

Based on the theories described in Chapter 2, a new axisymmetric viscous transonic flow solver (named AMIS) has been developed in the course of the thesis research. In this chapter, AMIS is validated through comparisons with quasi-1D nozzle theory and NASA experiments by Re *et al.* [40]. Then, cases of extreme operating conditions are simulated and examined, to explore the limits of AMIS.

Also, the design capability already proven by earlier two-dimensional Newton solvers is demonstrated through a re-design of nacelle cowl surface, operating at speed over the drag-rise Mach number.

4.1 Laval nozzle

The purpose of this section is to check the validity of inviscid transonic solutions, and the ability to handle a fully choked flow. The geometry of the axisymmetric Laval nozzle is described in Figure 4-1, which shows the (120x10) grid model of the nozzle. Grid clustering is done in the area where a shock is expected.

Figure 4-2 shows the stagnation density in the flow-field. Shock location is in agreement with quasi-1D nozzle theory. Also, shock strength is predicted to within 1% of theoretical values, as can be seen in Table 4.1.

For transonic calculations, the maximum Newton correction to the density in a cell is limited not to exceed a fraction (typically 0.2-0.3) of the density value to prevent initial transient instability. The initial flat convergence of Figure 4-4 is a direct result of this density relaxation. The supersonic region grows during this flat iteration, which is an indication

of a shock moving toward the exit as iteration proceeds. As soon as the shock position is settled, quadratic convergence of the Newton method is recovered. Each iteration requires about 1.5 seconds of CPU time on a SGI Indigo-I RS4000 machine.

As an initial flow condition, incompressible uniform density flow is used for $\frac{p_t^{inlet}}{p_{exit}} = 1.117$. This is called a start from 'scratch'. For other cases, the pressure ratio is increased with the solution at a previous pressure ratio being used as the initial condition. While better initial density conditions can increase the pressure ratio value that can be started from scratch, efforts required to yield those refinements are often costly when the geometry and flow phenomenon become complicated.

Table 4.1: Stagnation density ratio across shock

$\frac{p_t^{inlet}}{p_{exit}}$	$(\frac{\rho_t^{exit}}{\rho_t^{inlet}})theory$	$(\frac{\rho_t^{exit}}{\rho_t^{inlet}})AMIS$
1.117	0.9614	0.9626
1.186	0.9130	0.9193
1.273	0.8593	0.8606
1.387	0.8029	0.8043
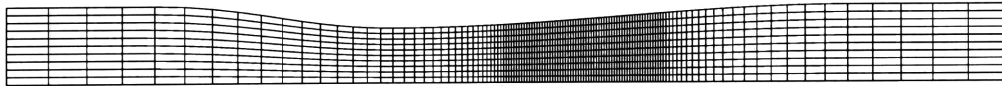
Figure 4-1: Computational grids for Laval nozzle

Figure 4-2: Stagnation pressure contours of Laval nozzle

dM = 0.05   1.0   **Theoretical Shock Location**
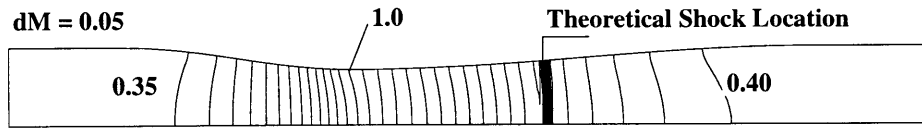
0.35   0.40

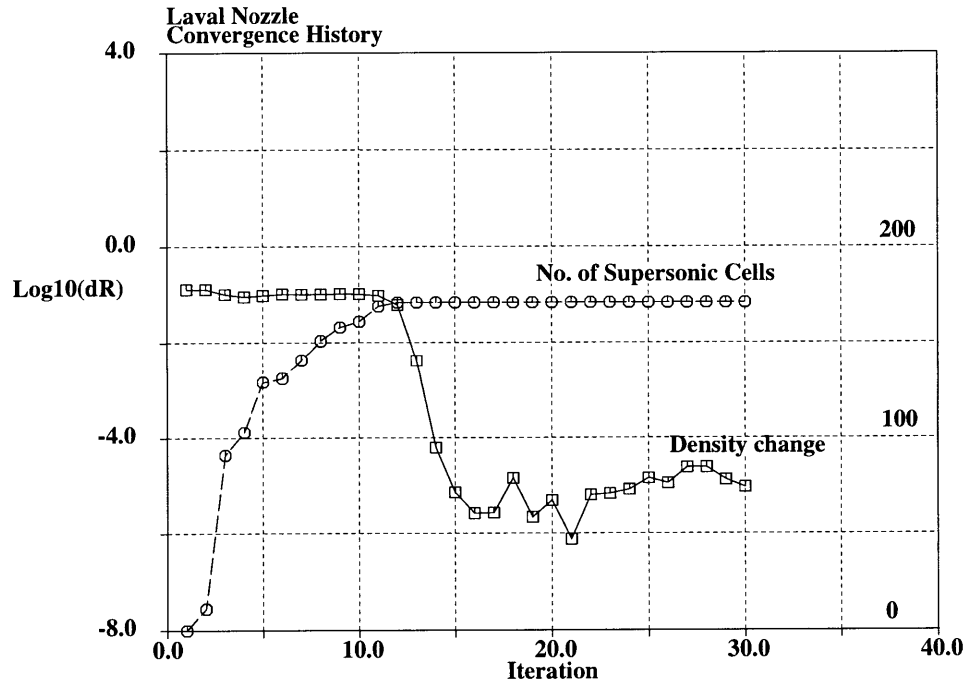Figure 4-3: Mach number contours of Laval nozzle

Figure 4-4: Convergence history of Laval nozzle

4.2 NASA axisymmetric cowls

This family of ellipse-nosed cowls were designed for a better off-design performance at transonic speeds than the popular and proven NACA-1 series cowls, without much reduction in the drag-rise Mach number.

'Cowl' refers to the external surface of a nacelle, while 'diffuser' refers to the internal contour. It is a legacy of the traditional nacelle design, to separate the geometry in several sections and match them together later. For example, forward cowl section is designed separately with the diffuser surface and the rear cowl section fixed. This approach makes a sense based on the observation that the diffuser does not affect the cowl aerodynamics very much as long as the mass flow ratio(MFR) is kept constant.

It is well known that a cowl lip with a sharper nose(smaller radius) provides lower cowl drag and higher drag-rise Mach number at the design cruise MFR. However, such a design often results in a poor performance under crucial off-design conditions. For example, high MFR engine operation during taxing and take-off requires the flow to turn around the cowl lip from the stagnation point on the cowl surface. The cowl lip with a smaller radius increases the adverse pressure gradient, and thus, is more vulnerable to the flow separation. In history, the initial sharp-nosed cowl design of the Boeing 747 had to be smoothed due to engine stall problems during taxing, at the expense of increased cruise drag of the nacelle. A similar situation occurs when the engine is idling or stalled, which is characterized by very low MFR. The flow is forced to turn around the lip from the stagnation point on the diffuser surface, leading to shocks and shock-induced flow separations on the cowl surface.

The experiments (Re *et al.* [40]) were purported to investigate the aerodynamic characteristics of three cowls with a common diffuser, and to validate the ideas behind the designs. In experiments, 'cowl' usually refers to the forward section which ends at the maximum cowl diameter, which is the case of the experiments cited here. Those three cowls were designated as short/medium/long cowls, based on the cowl length which also represents the design cruise Mach number of the cowl. Longer cowl is thinner and is designed for a higher cruise Mach number.

With larger cowl lip radii than the NACA-1 family, ellipse-nosed cowls were designed to delay the shock formation and shock-induced flow separation on the cowl surface during

the low MFR conditions. The smoothed nose also has a similar favorable effect on the high MFR performance, by retarding the shock formation and shock-induced flow separation on the diffuser surface to higher MFR compared to a NACA-1 series cowl of the same thickness ratio which is defined as the ratio of maximum cowl diameter to the cowl length.

Pressure measurements were made for each cowl in the NASA Langley Research Center 16-Foot Transonic Wind Tunnel, which is a single-return atmospheric wind tunnel with continuous air exchange. Mass flow ratios ranged between 0.27-0.87 for each Mach number of ranged 0.6-0.92. Maximum blockage effect of the model was 0.88%, which is discussed in section 4.2.2. For detail data of the wind tunnel, refer Corson *et al.* [12]. The cross-sectional description of the experimental model is shown in Figure 4-5 [40] , along with physical dimensions. Note the movable plug used to control the mass flow ratio. The boundary layers were tripped on both surfaces, at 0.6 inch after the cowl lip and at the geometric diffuser throat location, by applying a 0.10 inch strip of 120 silicon carbide particles. Reynolds number per foot ranged between $3.2\text{-}4.2{\times}10^{6}$, depending on the Mach number.

Of the experimental results, three cases are chosen to validate AMIS results : first, design mass flow ratio with design Mach number, second, low mass flow ratio with design Mach number, and finally, design mass flow ratio with high Mach number. The basic idea behind this is to cover a wide range of engine operating conditions. The first represents the optimal cruise condition, the second corresponds to an idling or stalled engine with feathering fan, and the third simulates an aircraft flying beyond the drag-rise Mach number. In addition to the matching of the experimental results, the cowl surface is re-designed to reduce shock strength of the third case, as a demonstration of design capabilities. The last example is a powered nacelle simulation at take-off condition, which is characterized by high MFR and low Mach number.

The grid modeling of the NASA short cowl is shown in Figure 4-6, which is actually a converged solution at cruise condition. All presented results are for the short cowl, because the effects of changes in Mach number and MFR can be shown most clearly by using the same cowl geometry. The number of stream-surfaces is set at more than required for engineering accuracy of the axisymmetric solution, to mitigate grid related problems of linearized three-dimensional solutions.

Dense contour lines at the center of the nacelle in Figure 5-8 shows a negatively-working actuator disk employed to match the MFR values of the experiments. Almost all calculations are done with viscous boundary layer coupling, although it has been observed that there is virtually no difference between inviscid solutions and viscous solutions when there is no strong shock or separation. The boundary layers are tripped at the same location as the experiments.
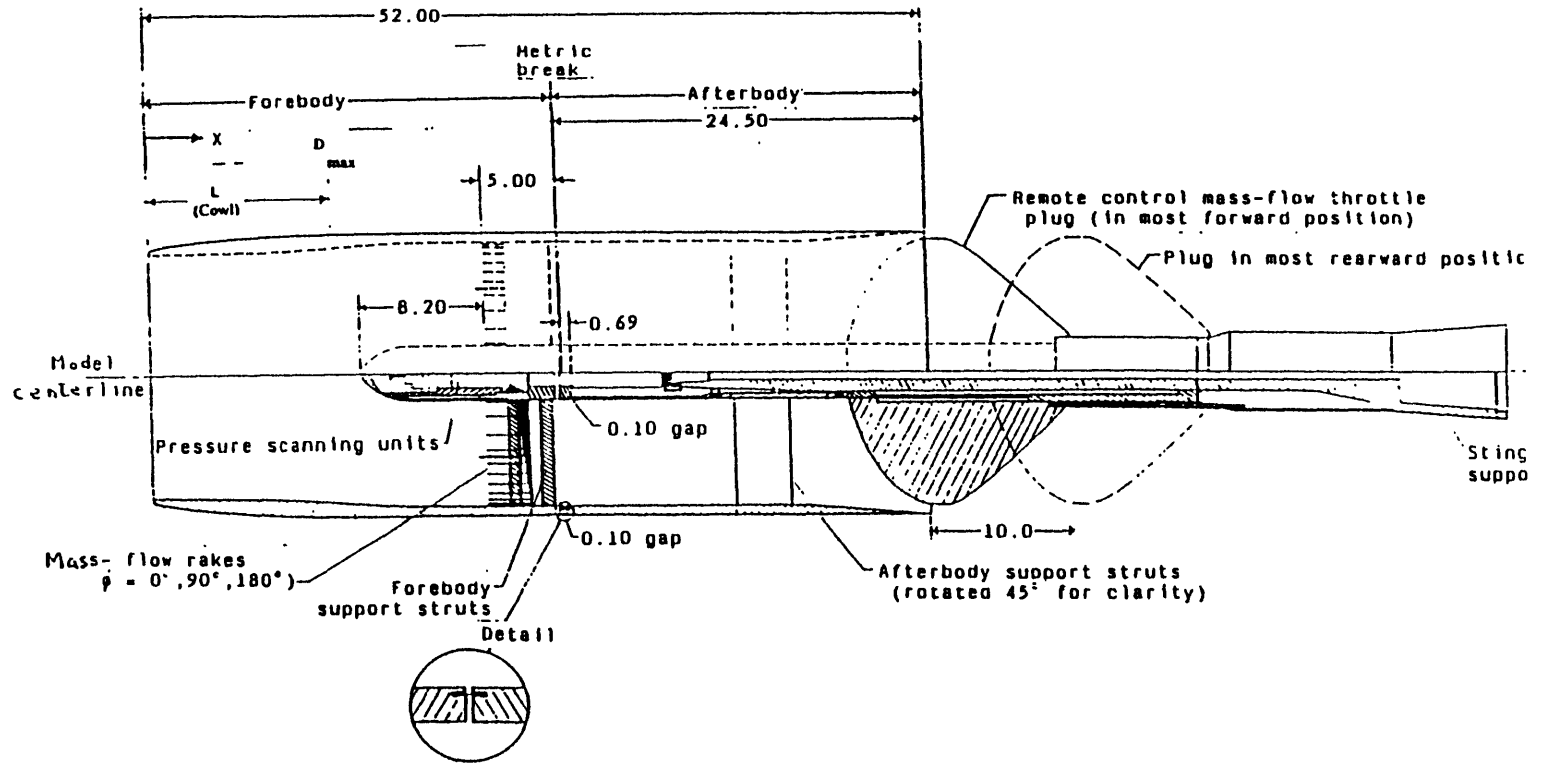
4.2.1 NASA cowl at cruise condition

At this condition, results of AMIS very closely follow the experimental C_p data points of Figure 4-7, even the small wiggle right after the cowl lip, where a discontinuity in surface curvature is suspected.

For a typical transonic flow case, about 15 Newton cycles are required for full convergence from an initial condition which is typically within 0.1 both in Mach number and MFR. For a fully subsonic flow, about 9 cycles are required. The difference is attributed to a moving shock location in transonic flow. The introduction of fan strength variable degrades the quadratic convergence of Newton system as mentioned in section 2.5, down to a 2^{-n} reduction rate , shown in Figure 4-8. Solutions of engineering accuracy (10^{-3}) are usually obtained within 6-7 cycles, which equals to 1.5 minutes on a SGI Indigo-I RS 4000 machine. Actually, the CPU time and memory requirements can be reduced to half when the axisymmetric solution is all that is wanted. Usually, 10 stream-surfaces are enough for a passage, but are doubled in the outermost passage for the purpose of linearized three-dimensional solutions.

4.2.2 NASA cowl with low MFR

The low MFR condition represents a stalled or idling engine, which swallows a small fraction of design mass flow. Stagnation point moves farther along the diffuser surface, and the spilled flow experiences rapid acceleration as it follows the cowl lip and often goes supersonic, forming shocks on the cowl surface. These shocks contribute to drag in two ways : the first is related with stagnation pressure loss of shock which in turn reduces pressure recovery on rear contracting section of nacelles and thus, generates pressure drag, while the second is from thickening or separation of boundary layers, which also blocks complete pressure recovery. Unless the shock strength is strong enough (Mn$\geq$1.5), the second part plays a
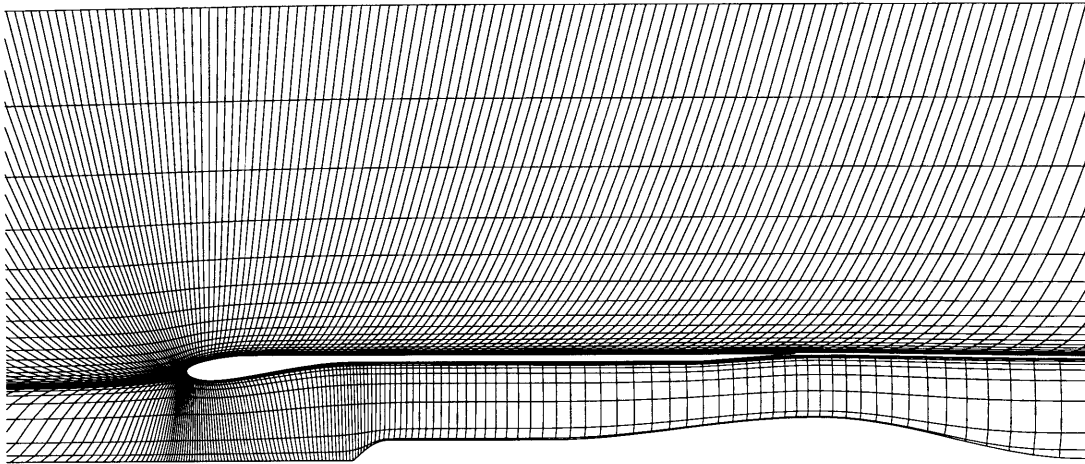
Figure 4-5: Configuration of NASA experimental model

Figure 4-6: Converged grids of NASA cowl,M = 0.74,MFR = 0.68(Cruise condition)

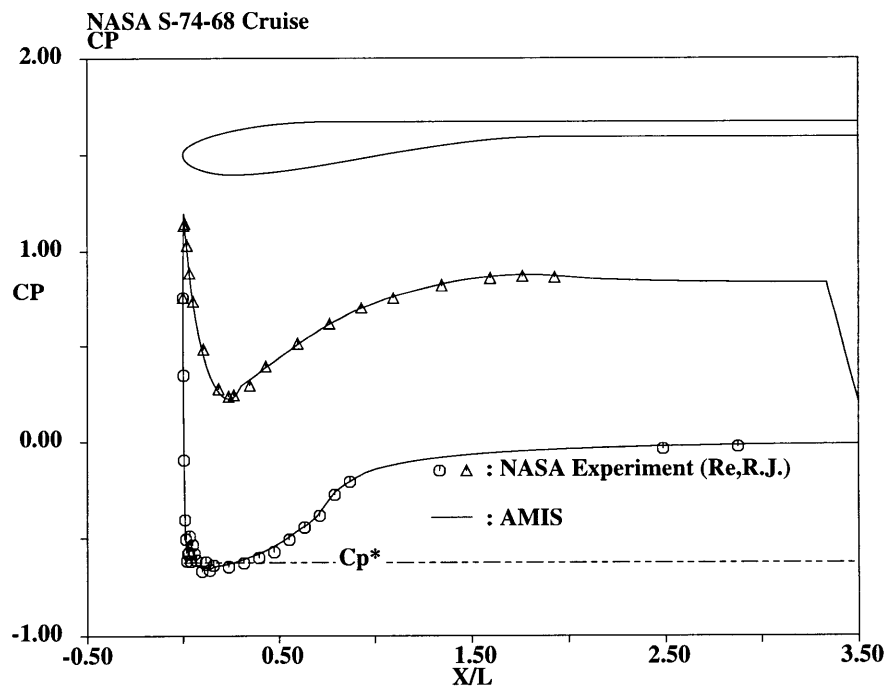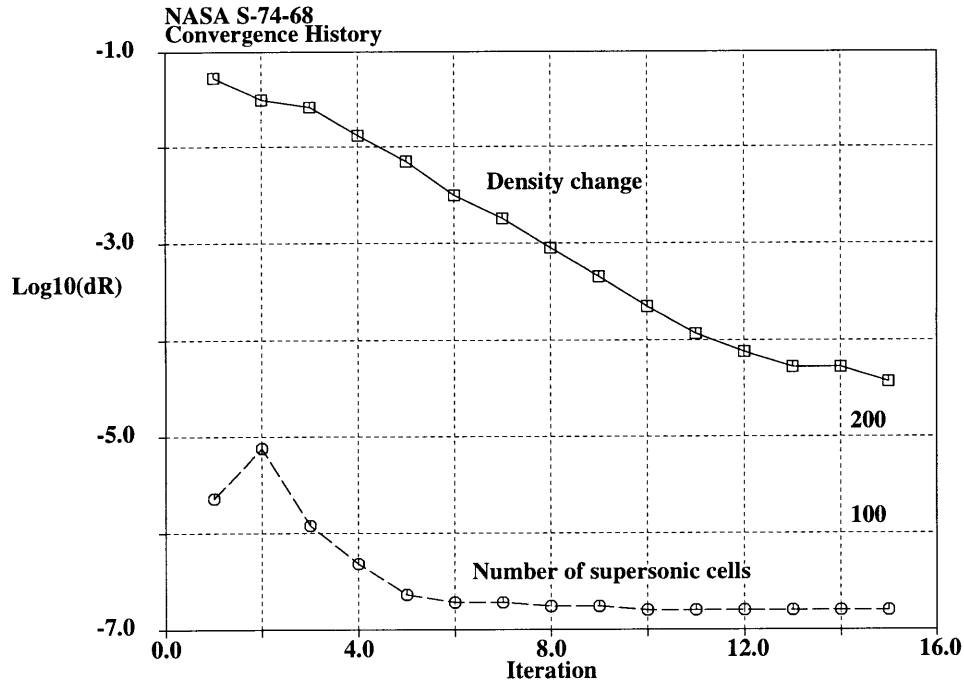Figure 4-7: C_p comparison of NASA cowl, M = 0.74, MFR = 0.68

Figure 4-8: Convergence of NASA cowl, M = 0.74, MFR = 0.68

major role, and weak shocks are considered to have more benefits than losses.

But, under the given experimental condition (M=0.74, MFR=0.27), the shock is strong enough to drive the boundary layer close to separation, shown in Figure 4-9 as a thickening δ^* gap. Also, the location of the stagnation stream-surface is noteworthy. To achieve low MFR operating conditions, a step by step reduction in MFR is taken from the initial geometry generated by stream-surface grid generator, like Figure 2-9.

Figure 4-10 shows a discrepancy between experiment and the computational result of matching the reported operation condition. Also plotted is a result of using a blockage-corrected operating condition, which fits the data better. In the experimantal low MFR condition, the blockage effect increases as more flow is spilled. Free stream Mach number is adjusted to match the resultant area ratio $\frac{A^*}{A}$ of isentropic flow theory (Liepmann and Roshko [34]). Also, MFR is adjusted to counter the increase in free stream Mach number. The stagnation density loss across the shock is shown on Figure 4-11.

4.2.3 NASA cowl surface design

At a Mach number greater than design speed, drag from shock wave formation rises rapidly and so does the thrust requirement. The surface design of this section is aimed at increasing
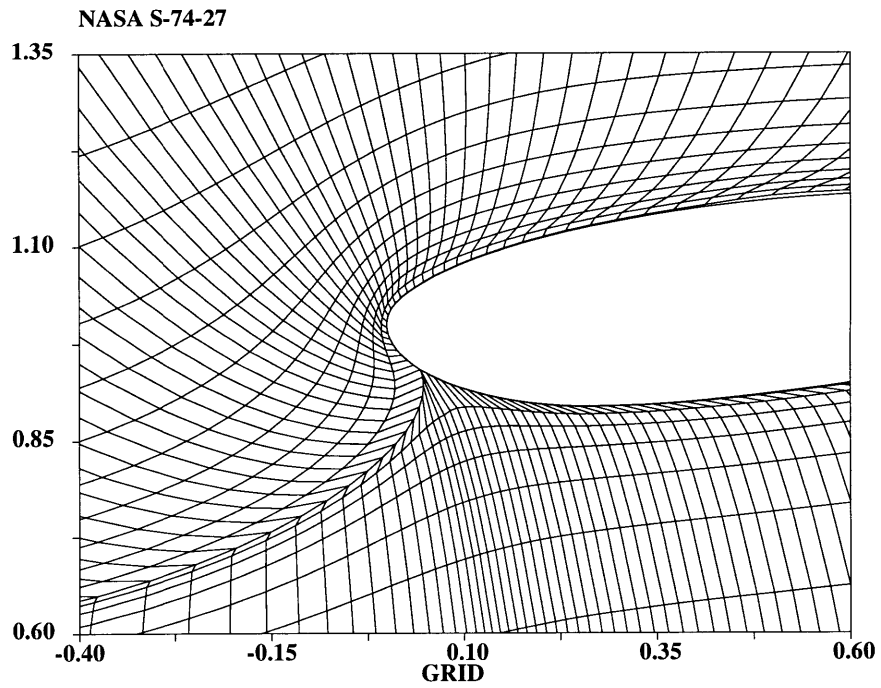
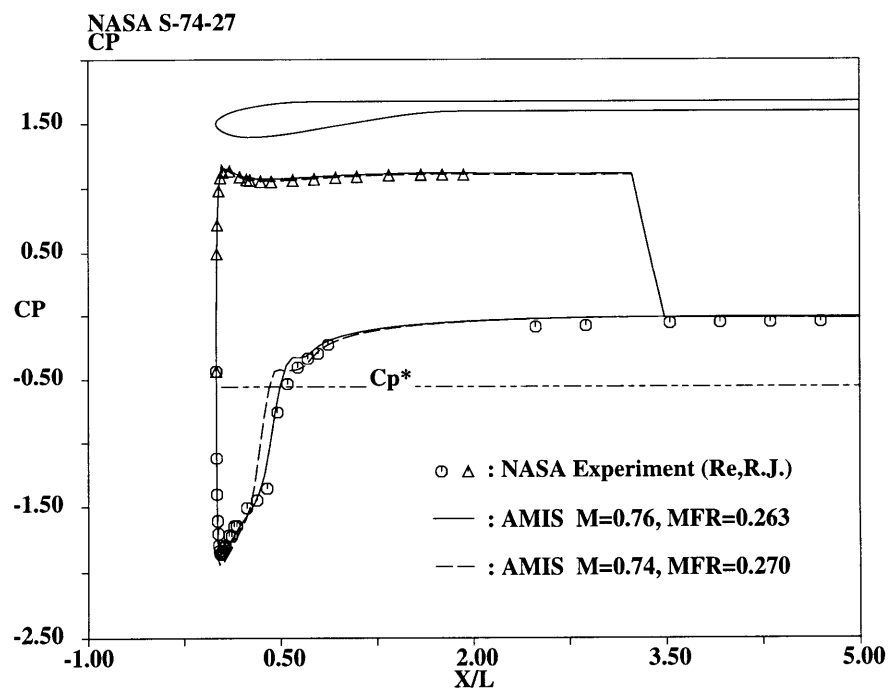Figure 4-9: Converged grids of NASA cowl, M = 0.76, MFR = 0.253

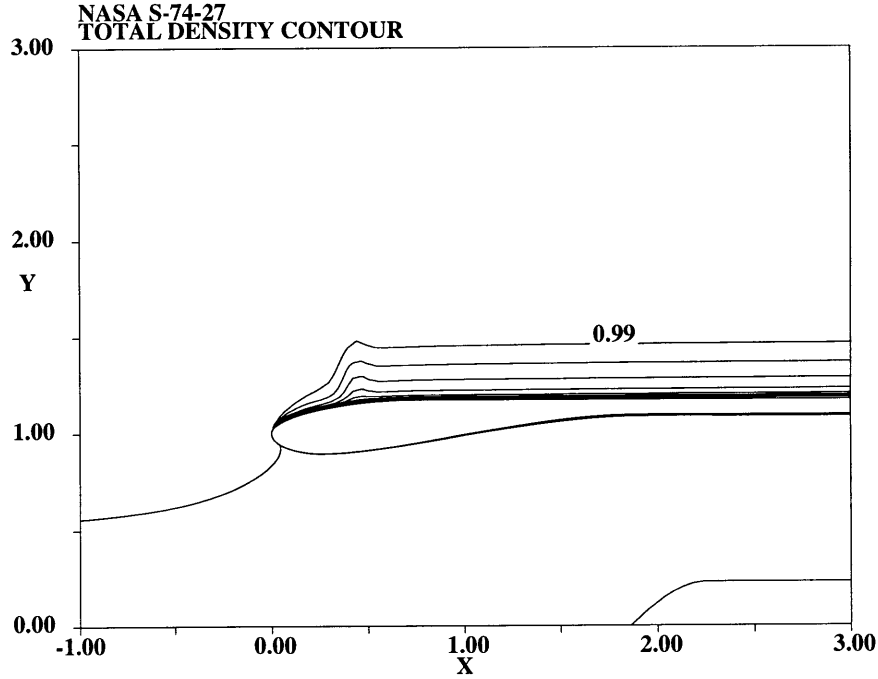Figure 4-10: C_p comparison of NASA cowl, M = 0.76, MFR = 0.253

Figure 4-11: Stagnation density of NASA cowl, M = 0.76, MFR = 0.253, $d(\frac{\rho_t}{\rho_{t\infty}}) = 0.01$

the drag-rise Mach number through the application of modal inverse design discussed in section 2.9. As the starting solution, the flowfield of the NASA short cowl at M=0.84, MFR=0.68 is used, while C_p result of M=0.80, MFR=0.68 is used to specify the inverse design pressure. Figure 4-12 shows the designed geometry , which gets thinner than the original surface. This is in line with an experimental correlation of drag-rise Mach number by Butler [9], which is $(r_{max}^2 - r_h^2)^{1/2}/L$, where r_{max} is radius at the maximum thickness and r_h is lip radius, while L is length of cowl. That translates directly into a thinner nacelle for higher drag-rise Mach number.

Comparison of Figure 4-15 with Figure 4-16, along with Figure 4-13 shows that shock is virtually eliminated on the re-designed cowl surface. Also, plotting of δ^* in Figure 4-14 shows the effect of the re-design on boundary layers. On the original surface, adverse pressure gradient of the shock drives the boundary layer close to separation, which is somewhat relieved by the radius change which thins the axisymmetric boundary layer. With the absence of a shock on the re-designed cowl surface, the boundary layer grows smoothly, resulting in a smaller wake thickness and less drag.
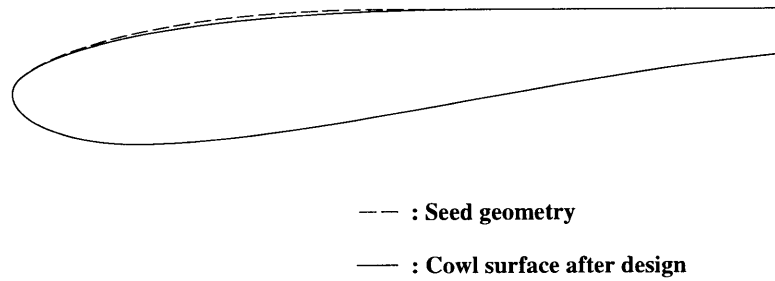
— — : Seed geometry

——— : Cowl surface after design
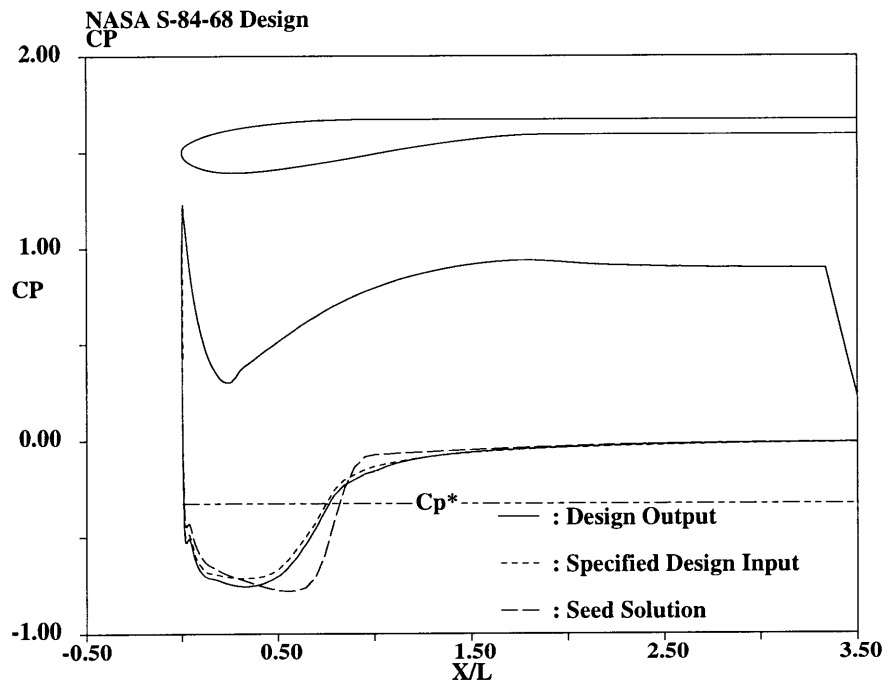
Figure 4-12: Cowl geometry after design

Figure 4-13: C_p on NASA cowl after design, M = 0.84, MFR = 0.68
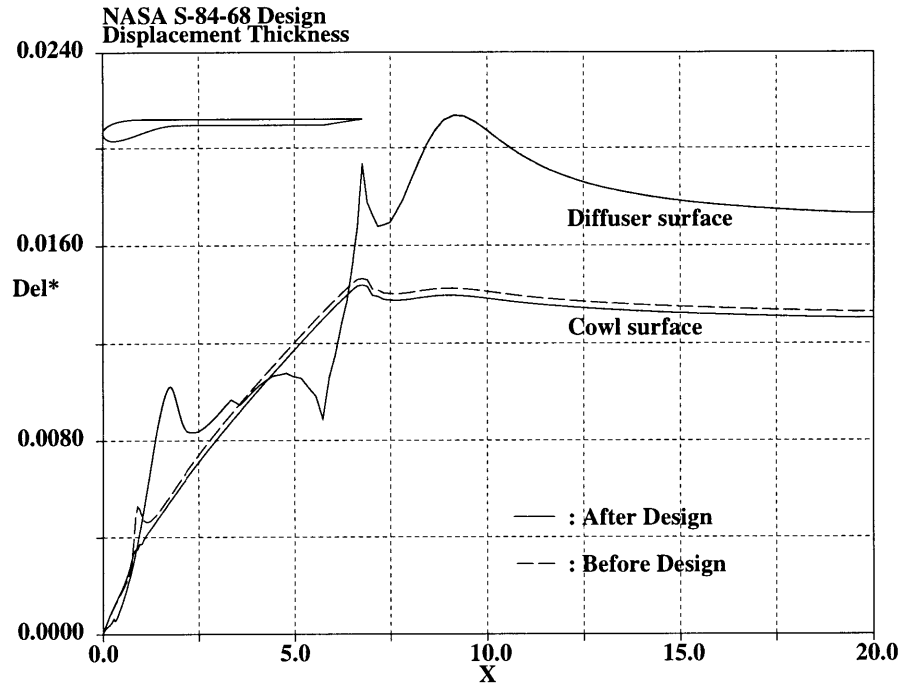
68

NASA S-84-68 Design
Displacement Thickness

Figure 4-14: Displacement thicknesses after design, M = 0.84, MFR = 0.68

4.2.4   NASA cowl with high MFR

High MFR occurs during take-off when an engine needs more air than the flight speed and the frontal nacelle area can provide. Under this condition, the worst possibility is the flow separation on the diffuser surface which also can cause the engine stall.

The purpose of this example is to test a positively-working actuator disk. Unlike previous cases, where the fan had to work negatively to restrict mass flow into the nacelle, the fan should work positively to suck the flow in. As in the case of the low MFR condition, leading edge movement like Figure 4-17 is achieved through gradual change in mass flow ratio. Unfortunately, the author failed to find experimental data of powered axisymmetric nacelle that could be compared.

Note the rapid change of C_p in Figure 4-18. With the help of streamline divergence on diffuser surface, which plays the same role on cowl surface, the boundary layer is healthily attached in spite of the severe adverse pressure gradient.
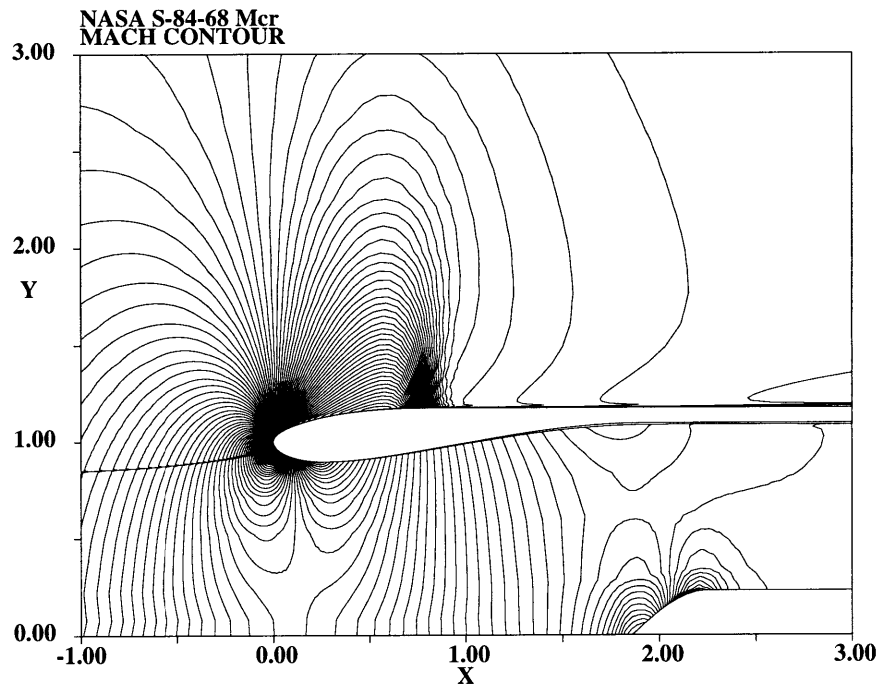
69

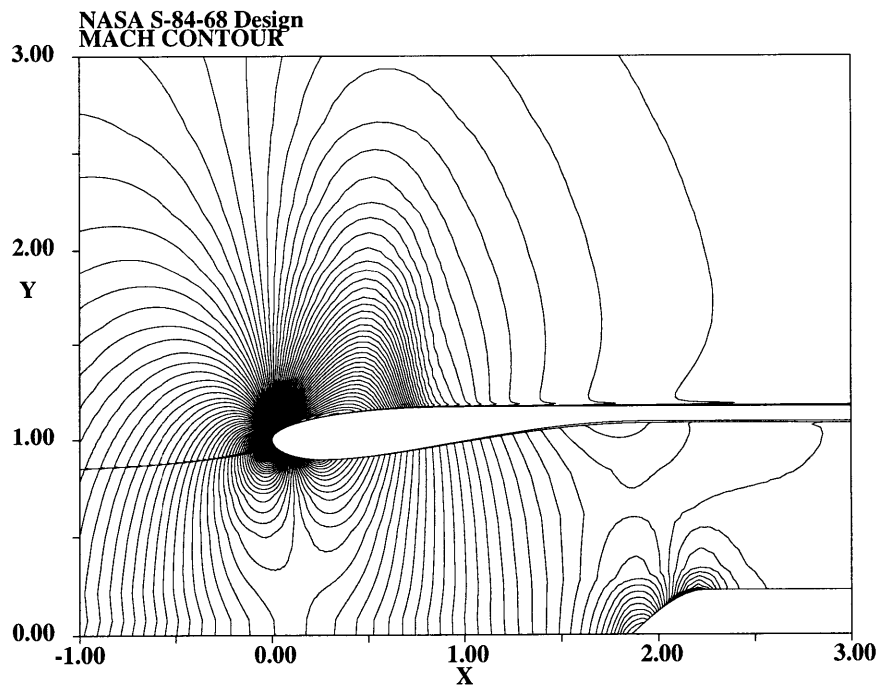Figure 4-15: Mach number contours before design, M=0.84,MFR=0.68 (dM=0.01)

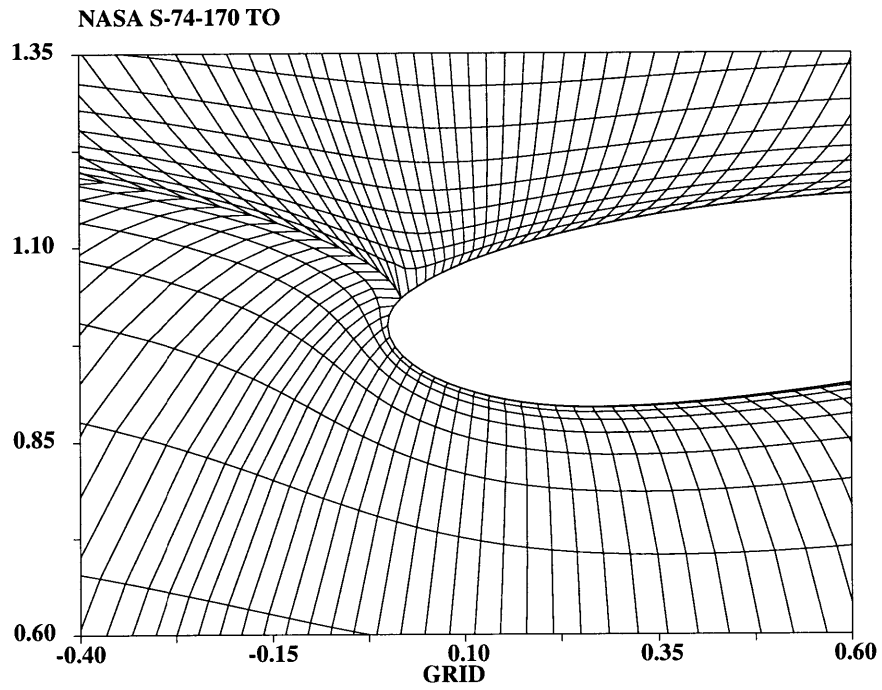Figure 4-16: Mach number contours after design, M=0.84,MFR=0.68 (dM=0.01)

NASA S-74-170 TO

Figure 4-17: Converged grids of NASA cowl, M = 0.20, MFR = 1.70
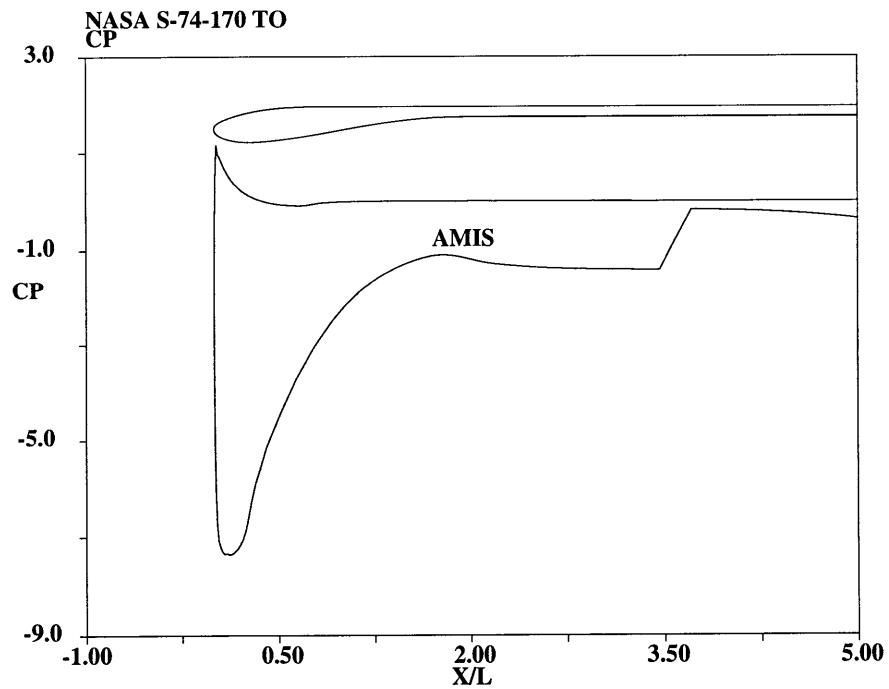
NASA S-74-170 TO
CP

Figure 4-18: C_p distribution on NASA cowl, M = 0.20, MFR = 1.70

Chapter 5

Linearized three-dimensional flow results

Following the approach of the previous chapter, the first section of this chapter validates the linearized three-dimensional flow solver (named LAMIS) which has been developed from the theories presented in Chapter 3, by comparing with theoretical results of Belotserkovskii [6]. The second section covers comparisons with NASA experiments of Re *et al.* [40]. All results presented in the second section are linearized solutions of axisymmetric results of section 4.2. Because the geometry of the nacelle is axisymmetric, only one first-order Fourier mode is required as the perturbation mode.

It has been observed that linearized solution is sensitive to grid related issues like grid skewness, aspect ratio, and grid size variation. To ease these, axisymmetric base solution is redone with less skewed grids which usually have more cell numbers. For example, the NASA cowl problem is redone on a (180x30) grid instead of a (160x20) grid which was enough to provide a nice axisymmetric solution , at twice the memory and CPU requirements.

Resource requirement increases relative to the axisymmetric problem are 2 times more memory and 8 times more CPU time. The memory increase is due to the increase in the variable number per cell, which is 2 to 3 (Chapter 4). The CPU increase is from the matrix size change and the increased number of global variables which are introduced to constrain instabilities. For the NASA cowl case, LAMIS requires 42MB of memory and 2.5 minutes on SGI Indigo-I RS4000, compared to 20MB and 17sec/cycle for the axisymmetric problem.

5.1 Thin annular wing with incidence

The thin annular wing has been the workhorse test case since the beginning of this work. It represents all aspects of three-dimensional problems, and its simplicity has helped in differentiating perturbation model problems from computational problems like grid skewness, grid resolution, and magnitude of the finite perturbation. Belotserkovskii [6] did an extensive work on this problem using the discrete vortex method. These results were validated through wind tunnel experiments that even included compressibility effects.

However, this simple geometry introduces one more unconstrained mode, due to the absence of a mechanism for controlling the axis streamline. To prevent this, the inflow position of the axis streamline is prescribed , resulting in conflict with the angle constraint, Equation (3.28). This leads to a poorly constrained angle mode in the axis streamtube, affecting the entire flowfield through interaction between modes. Untidy swirl velocity contour lines near the axis in Figure 5-1 are considered to stem from this conflict. Note that swirl velocity is plotted on the symmetry plane where $\sin \phi$ is zero by definition. It is done for visualization purposes only, and note that swirl velocity on that plane is zero. Also, its value is scaled to $\alpha = 45^o$, which gives $\tan \alpha = 1.0$, for a comparison with the theoretical results.

To facilitate comparison with the results of Belotserkovskii [6], it is necessary to derive a relation between swirl velocity and lift coefficient of an annular wing. The former is the result of LAMIS and the latter is the main concern of the theoretical work. By definition, the strength of an annular vortex sheet is the swirl velocity jump across it.

$$\gamma = (w^+ - w^-)\sin \phi = \frac{1}{R}\frac{d\Gamma}{d\phi} \tag{5.1}$$

where R is the radius, C is the chord length of an annular wing.

Then, the relation between γ of the vortex sheet and C_L of the annular wing becomes

$$(w^+ - w^-) = -C_L\frac{UC}{\pi R} \tag{5.2}$$

For the swirl jump of $1.47U$, where $C = R$ (Figure 5-1), the lift coefficient predicted by LAMIS is $C_L = 1.47\pi = 4.62$. When $\tan \alpha = 45^o$, C_L becomes the same as the lift coefficient slope $C_{L\alpha}$, due to the assumption $\tan \alpha = \alpha$ in the linearization process.

73

Following these procedures, lift coefficients predicted by LAMIS are compared to results of Belotserkovskii [6] in Table 5.1. As can be seen, LAMIS predicts up to 96% of the theoretical lift. Based on the observation that the magnitude of pressure correction does not change the solution significantly (around 1%), the difference is considered to come from the constraint of the axis streamline. Also, a part of the difference is attributed to the finite grid resolution around the sharp leading edge where a singular solution is expected. The lift can also be calculated with pressure integration on the wing surface. This lift has been observed to match the lift calculated from vorticity to within 2%.

In the presence of wing lift, the flow gets a downwash, shown as the deflection of nacelle flow passage in stream-surface grids of Figure 5-1. In the pressure contours of Figure 5-3, lines near the flow passage interface represent non-dimensionalized free stream pressure $p_\infty = 1.0$. These are especially noticeable on inflow and outflow boundaries. Similar to those lines, zero swirl lines are also found in Figure 5-1. This suggests that constraint given by Equation(3.28) is adversely affecting the solution near passage interface where cells have very high aspect ratio.

For all annular wing problems, M=0.2 is used. The insensitivity of the lift coefficient to Mach number change (up to .6) was observed by Belotserkovskii [6], which also has been observed by the author. It is attributed to the increase in the effective wing aspect ratio λ due to the lengthening effect of compressibility, which cancels the increase in C_p.

Table 5.1: Comparison of lift coefficient slope $C_{L\alpha}$

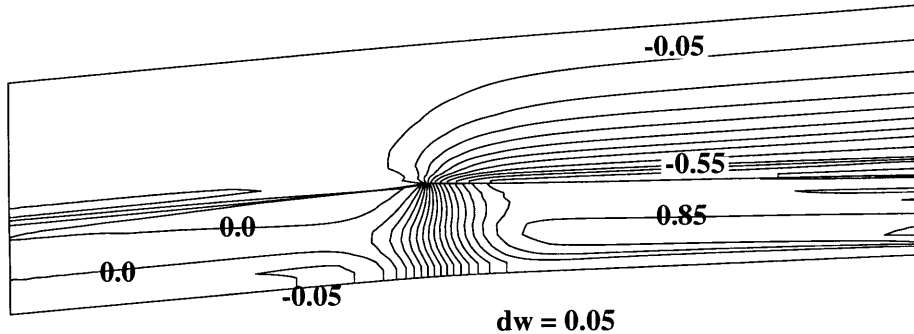| $\lambda = Diameter/Chord$	$C_{L\alpha}$ [6]	$C_{L\alpha}$ (LAMIS)
1.0	2.90	2.78
2.0	4.83	4.62
2.5	5.47	5.27
4.0	NA	6.18

$$dw = 0.05$$

Figure 5-1: Swirl velocity contours of thin annular wing, $dw = 0.05U$

5.2 NASA axisymmetric cowl with incidence

During the wind tunnel experiments , Re. *et al.* [40] also measured C_p and the lift of the nacelle subject to an incidence angle for selected Mach numbers and MFR's. But, the lift data were regarded uacceptable by the authors due to the failure of the sting balance during experiments. Thus, like axisymmetric flows, only surface C_p are compared with experiments.

5.2.1 NASA cowl at cruise condition, $\alpha = 3.0^o$

Angle of attack of this magnitude can represent several situations like an upward gust , slow climb , and an angle set by design. In linearized solutions, the magnitude of α is simply a scale factor applied to the computed α sensitivities. The assumption behind linearization theory is small α, typically $\tan \alpha < 0.1$. That corresponds to $\alpha < 5.7^o$, which contains the α range of experiments.

Figures 5-4, 5-5 show surface C_p distributions of LAMIS. On the lower cowl surface ($\phi = 180$), prediction follows experimental data faithfully, while LAMIS misses a small shock on the upper cowl($\phi = 0$). This is attributed to the absence of supersonic flow in the base axisymmetric solution as shown in Figure 4-7. The shifting in domain of influence
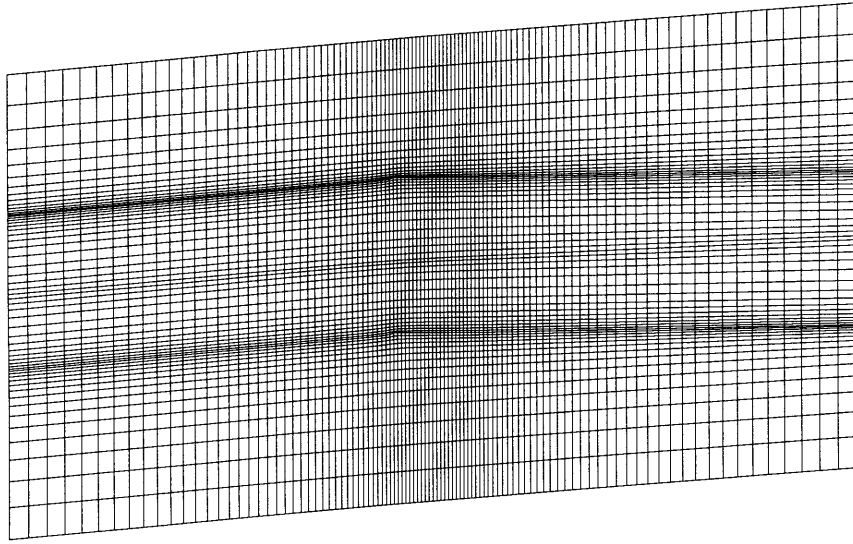
75

Figure 5-2: Solution grids of thin annular wing , $\alpha = 5^o$
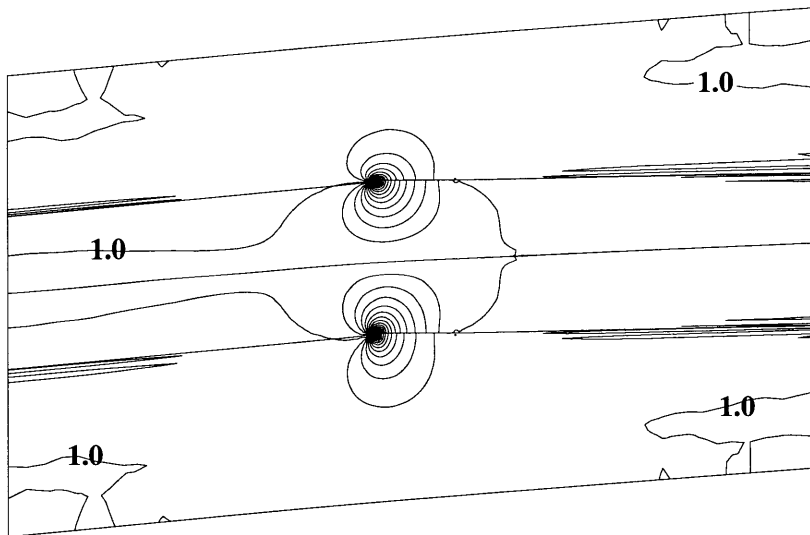

Figure 5-3: Pressure contours of thin annular wing , $\alpha = 5^o$, $dp = 0.01 q_\infty$

76

for supersonic flow can not be linearized properly because it relies on switching mechanism, which makes linearized solution less reliable where the local flow speed is close to Mach 1.

Inviscid solutions also shows good agreement with experiments and are barely distinguishable from viscous solutions, and thus are omitted here.

5.2.2 NASA cowl at high speed M=0.84, $\alpha = 2.0^o$

This section is intended to check the ability of LAMIS in predicting shocks. C_p comparisons of Figures 5-6, 5-7 show proper prediction in shock locations, although strength prediction shows 20% discrepancy in pressure drop on the lower cowl surface. On the upper cowl, LAMIS predicts the experimental data within 10%. The difference in strength of shocks between upper and lower cowl surface is clearly shown in Figure 5-8. The mismatching of pressure across the passage interfaces is the byproduct of pressure correction of Equation (3.29), which fixes the saw-tooth instability but also affects the angular stretching component of the angle mode (Figure 5-9). The pressure mismatch diminishes as the stream-surface approaches the leading edge, which is a sign of decreasing saw-tooth instability in the angle mode. As explained in section 3.10, this instability mode is suppressed near a body surface, which explains the nice surface pressure prediction of Figure 5-6 and the 'clean' swirl contours near body surfaces (Figure 5-1). The pressure correction also affects the downwash of the nacelle flow passage, shown as a flow deflection in Figure 5-10, which bends upward, unlike the straight deflection of Figure 5-2.
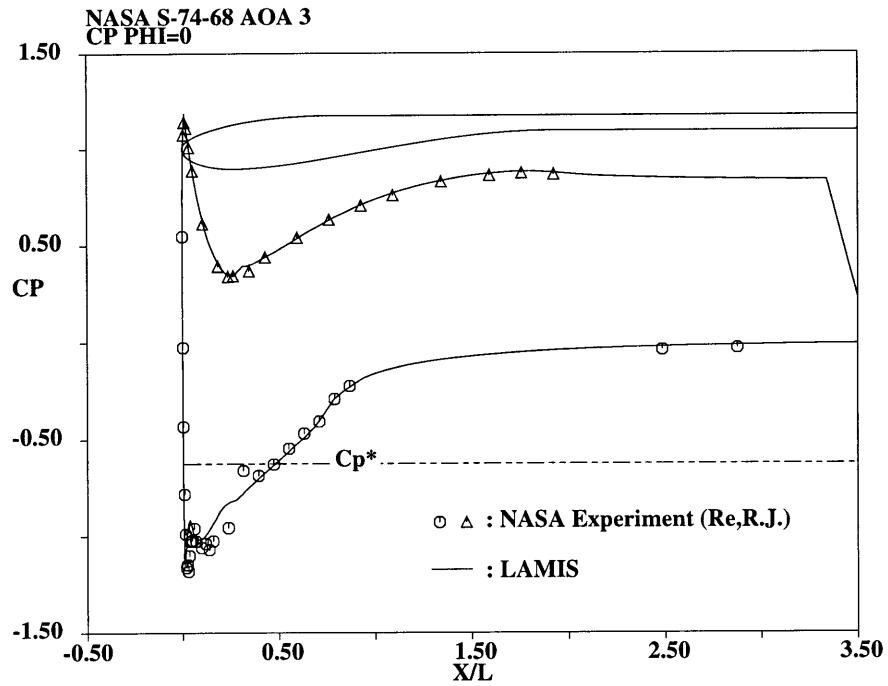
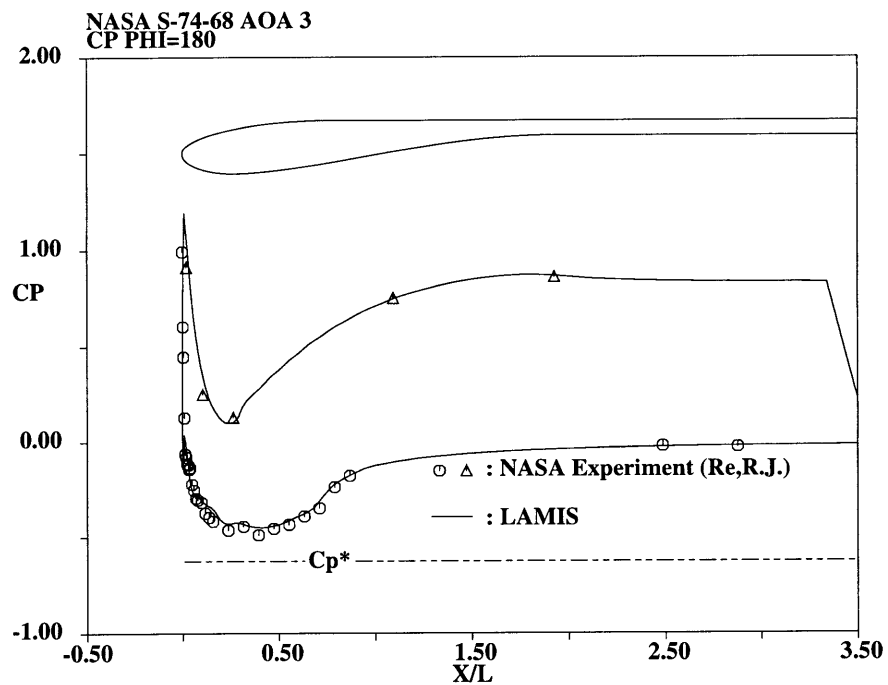Figure 5-4: C_p comparison of NASA cowl, M=0.74, MFR=0.68, $\alpha = 3.0^o, \phi = 0^o$

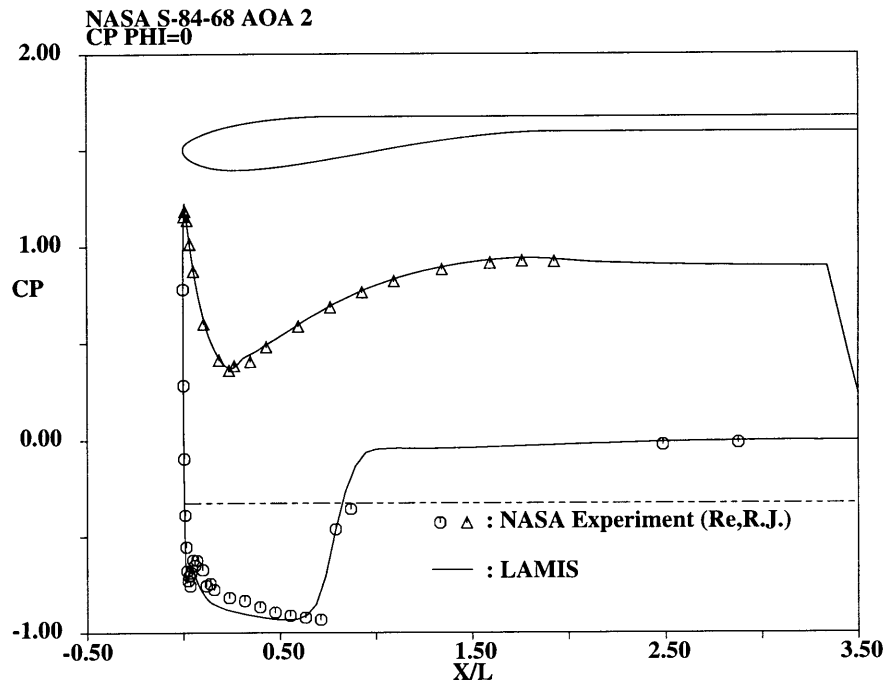Figure 5-5: C_p comparison of NASA cowl, M=0.74, MFR=0.68, $\alpha = 3.0^o, \phi = 180^o$

Figure 5-6: C_p comparison of NASA cowl, M=0.84, MFR=0.68, $\alpha = 2.0^o, \phi = 0^o$

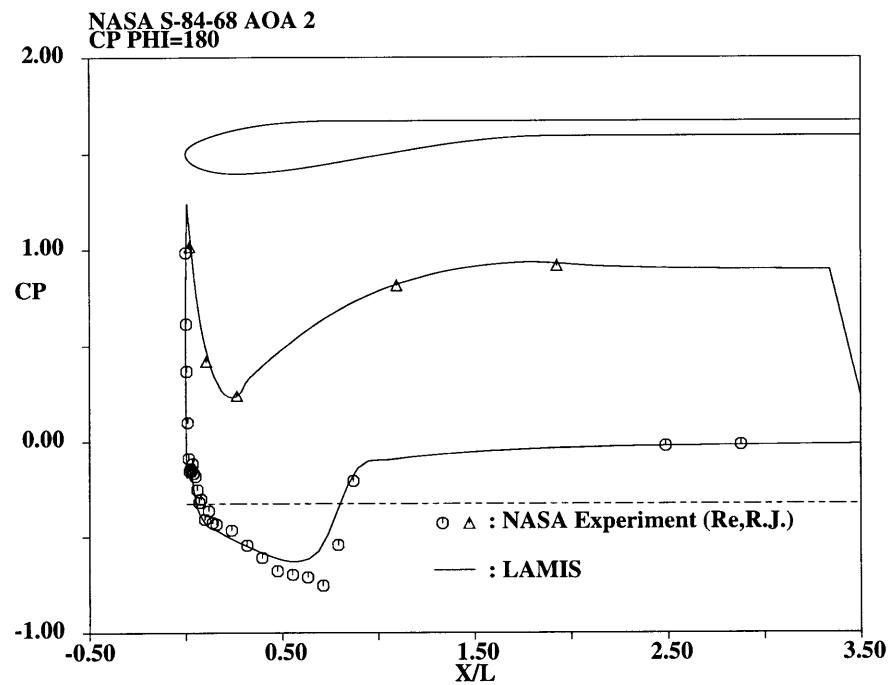

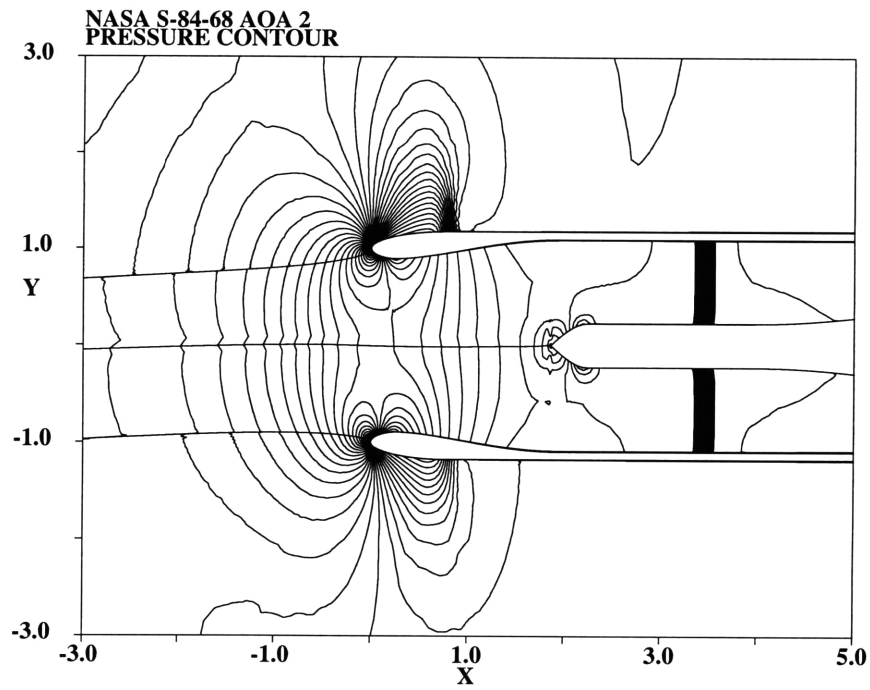Figure 5-7: C_p comparison of NASA cowl, M=0.84, MFR=0.68, $\alpha = 2.0^o, \phi = 180^o$

79

Figure 5-8: Pressure of NASA cowl, M=0.84, MFR=0.68, $\alpha = 2.0^o, dp = 0.01 q_\infty$
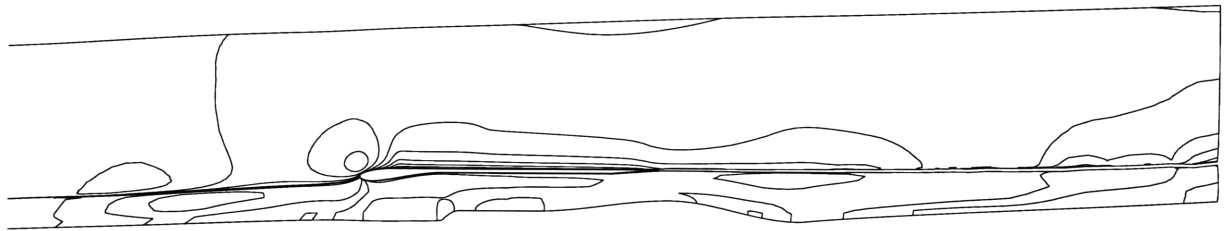

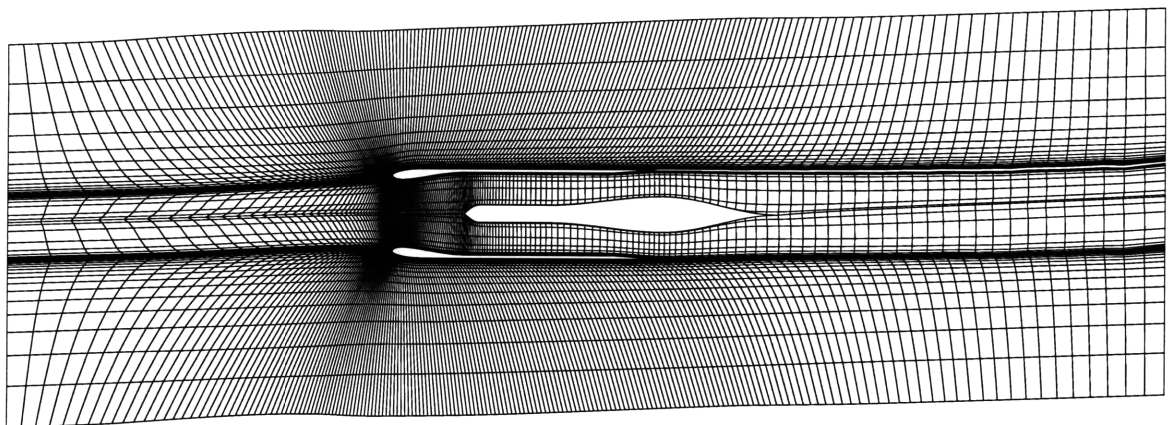Figure 5-9: Swirl velocity of NASA cowl, M=0.84, MFR=0.68, $\alpha = 2.0^o, dw/U = 0.01$

Figure 5-10: Solution grids of NASA cowl, M=0.84, MFR=0.68, $\alpha = 2.0^o$

5.2.3 NASA cowl with low MFR, $\alpha = 2.0^o$

The purpose of this section is to check the ability of LAMIS in handling skewed grids near the leading edge stagnation point. The base axisymmetric solution also introduces strong shocks, as shown in Figure 4-10. This poses a challenge to the boundary layers whose base solutions are already close to separation.

C_p comparisons of Figures 5-11,5-12 show proper prediction in shock strength. The step in experimental C_p (Figure 5-11) suggests a separation bubble in the boundary layer. The mismatching of LAMIS is considered to come from the unseparated base axisymmetric boundary layer. Like the upwinding switch in supersonic flow, the boundary layer closures change fundamentally when separation happens. Therefore, the behavior of a separated boundary layer can not be predicted properly through linear analysis when the base flow is attached. Also plotted are inviscid solutions, which suffer difficulty in matching solutions involving shocks. However, on the diffuser surface, there is virtually no difference between viscous and inviscid solutions. H_k plotting of Figure 5-13 explains the wiggle in C_p at $\phi = 180^o$. The boundary layer thickness is reduced in an exaggerated manner and causes locally accelerated flow. This is caused by the linearization near the transition location. As with separation, this is fundamentally non-linear.

The ability in handling skewed grids near the leading edge stagnation point is proven in Figure 5-14, which also shows a separated boundary layer.

5.2.4 NASA cowl with high MFR, $\alpha = 3.0^o$

This section checks the behaviour of LAMIS with a positively-working actuator disk. LAMIS has been observed to have no difficulty, and shows the same trend of attenuating downwash (Figure 5-15) explained in section 5.2.2.
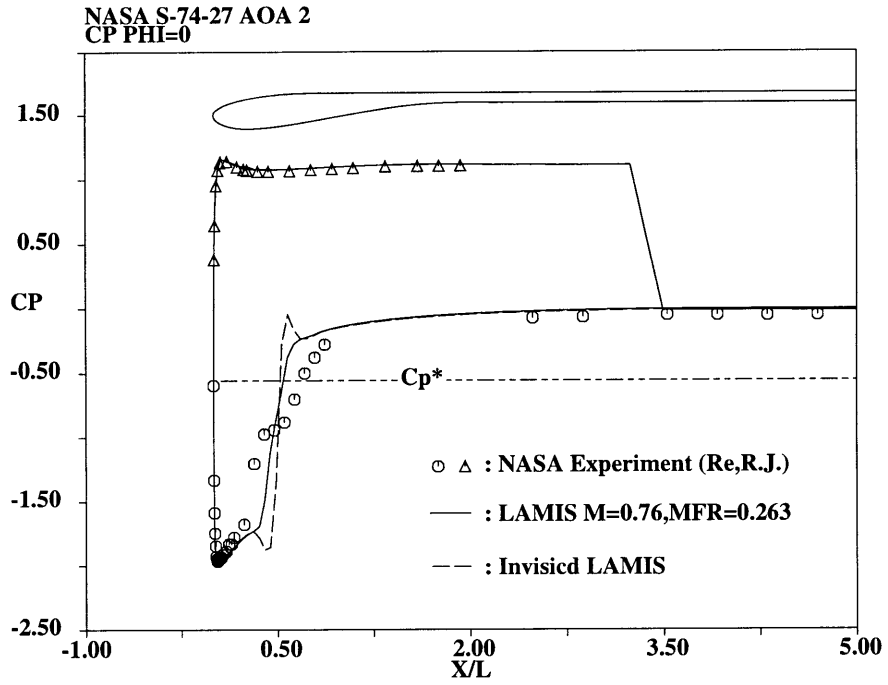
Figure 5-11: C_p comparison of NASA cowl, M=0.76, MFR=0.263, $\alpha = 2.0^o, \phi = 0^o$
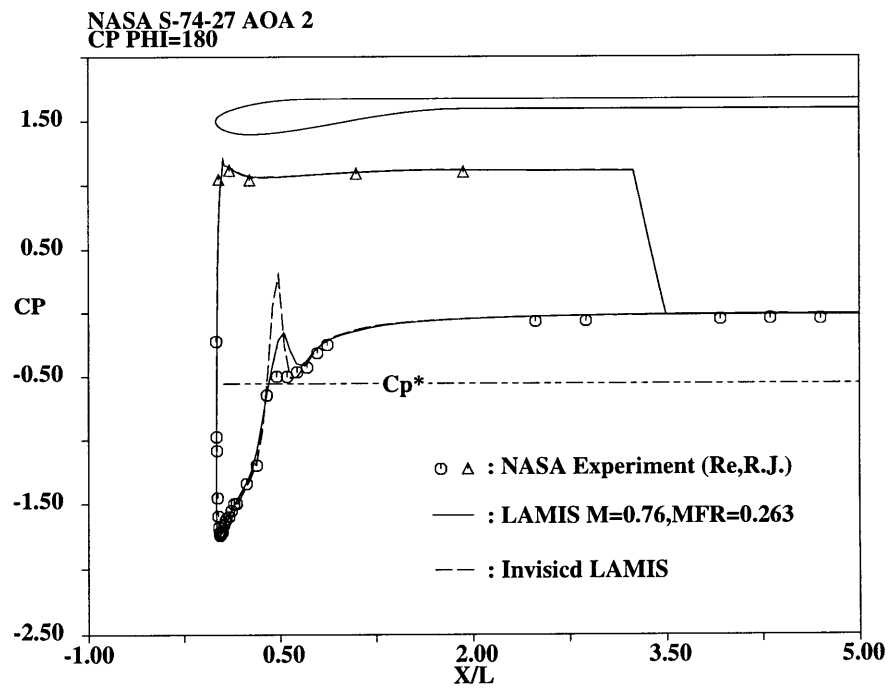

Figure 5-12: C_p comparison of NASA cowl, M=0.76, MFR=0.263, $\alpha = 2.0^o, \phi = 180^o$
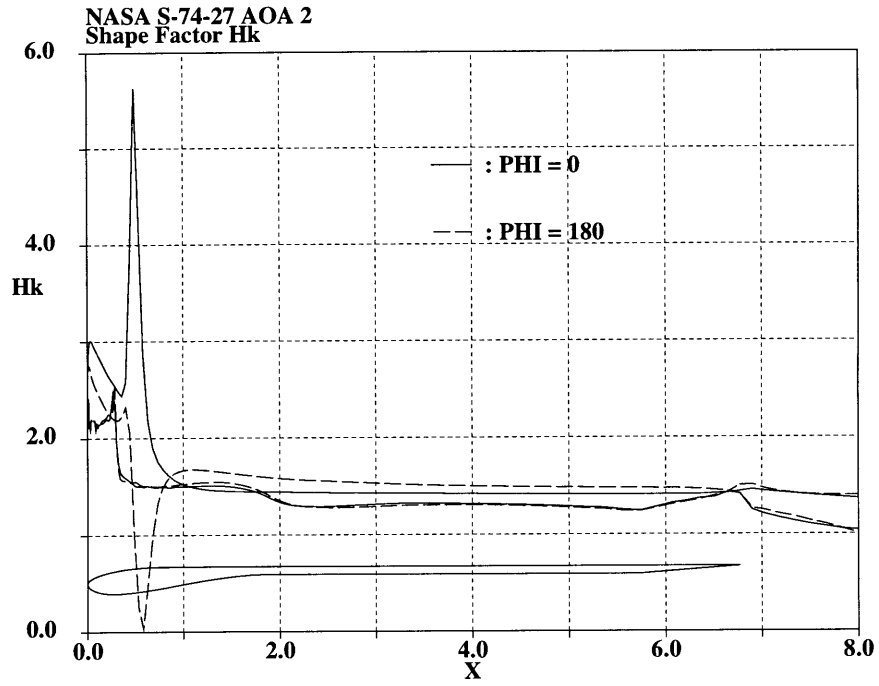
Figure 5-13: Shape factor H_k of NASA cowl, M=0.76, MFR=0.263, $\alpha = 2.0^o$
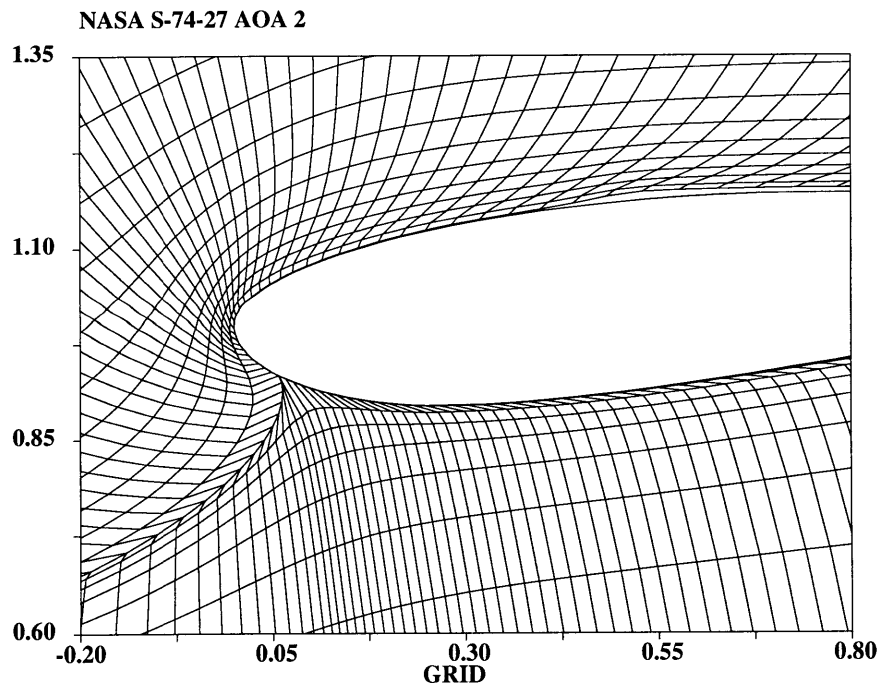

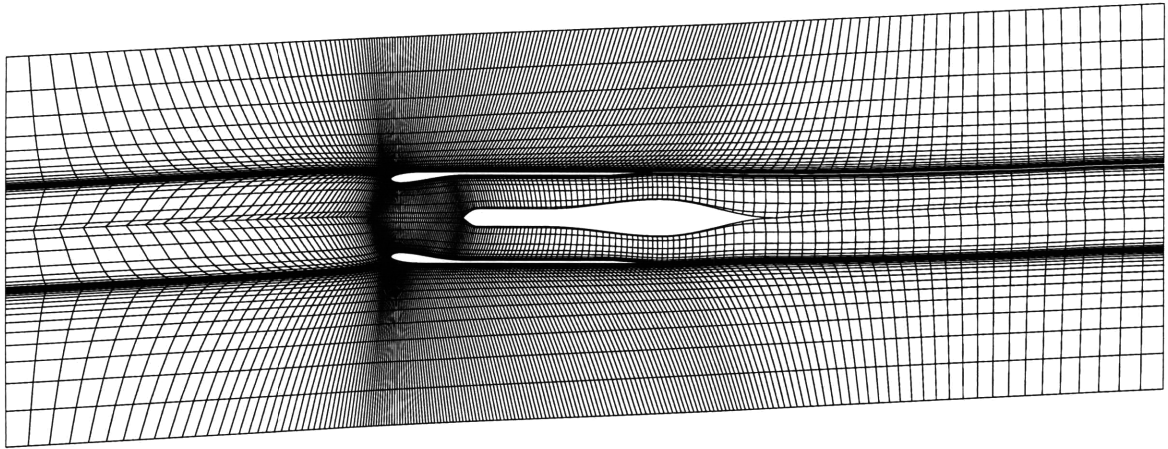Figure 5-14: Grids around NASA cowl lip, M=0.76, MFR=0.263, $\alpha = 2.0^o, \phi = 0^o$

Figure 5-15: Solution grids of NASA cowl, M=0.20, MFR=1.7, $\alpha = 3.0^o$

Chapter 6

Conclusions and

Recommendations

6.1 Conclusions

6.1.1 Axisymmetric flow solver

The stream-surface based Newton approach of Drela [17] and Giles [19] has been successfully applied to the non-swirling axisymmetric flow problem. The resultant code, named AMIS, has been validated through comparison with theoretical results and experiments, and retains the fast convergence properties of the Newton method. A typical transonic nacelle flow calculation requires 4 minutes of CPU time and 20 MB of memory on a workstation(SGI Indigo-I).

6.1.2 Axisymmetric boundary layer

The integral forms of the axisymmetric boundary layer equations are coupled to inviscid Euler equations, with two-dimensional closure and transition relations of Drela [17]. On the cowl surface of a nacelle, increasing radius delays layer growth by the stretching effect.

6.1.3 Actuator disk modeling of fan

The fan is modeled as a single actuator disk with the stagnation enthalpy and stagnation density jump. The actuator strength can also be used to control mass flow ratio of an engine, although it degenerates the quadratic convergence of Newton method, resulting in

twice the CPU time of a non-controlled case. This capability has been demonstrated by matching mass flow ratios of experiments. Also, a powered nacelle simulation has been demonstrated.

6.1.4 Streamline grid generation

An initial streamline grid generation method has been applied to the axisymmetric flow problem. During this process, an axisymmetric potential solver based on the panel method was constructed. Grids generated by this technique have helped in stabilizing initial transients of the Newton method.

6.1.5 Linearized three-dimensional flow

A linear perturbation approach has been developed to predict weakly three-dimensional(quasi-3D) flows around axisymmetric bodies. The base axisymmetric flow is assumed to be non-swirling. Three first-order Fourier geometric perturbation modes are formulated to linearize the movement of axisymmetric stream-surfaces, which offer features useful to engine nacelle design. The formulations can be extended to the higher order Fourier modes, which enables the application of the linearization theory to the non-axisymmetric geometries which are close to axisymmetry.

The resultant code, to be named LAMIS, has been demonstrated to match theoretical results and empirical data for the three-dimensional flow around axisymmetric bodies. A typical transonic nacelle flow calculation requires 2.5 minutes of CPU and 42 MB of memory on a workstation(SGI Indigo-I).

6.1.6 Limitations of the linearization approach

It has been observed that highly non-linear flow phenomena can not be predicted correctly by the linearization approach developed in this thesis. Three such non-linear phenomena have been confirmed, which are : shock formation from a subsonic flow, boundary layer separation from an attached flow, and significant transition movement.

6.2 Recommendations

6.2.1 Fan modeling

For a better simulation of an engine and fan cowl, the modeling of multiple disks is recommended. Also, a proper scheme is required to distribute the strength over multiple disks, which can simulate wide chord fan blades. This feature will help an accurate prediction of the average stream-surfaces and their application to the spanwise design of the fan blades.

6.2.2 Isolated engine simulation

AMIS has the capability of modeling multiple flow passages, of which there are 2 in most engines. Through the addition of one more flow passage and the modeling of the engine core flow, a full simulation of an isolated engine operation can be effectively made. Thus, the nacelle can be designed with consideration of influences from the engine core and fan. Also, by fixing the far-field stream-surface, wind tunnel experiments can be simulated.

6.2.3 Swirl velocity in axisymmetric flow

AMIS excluded the ϕ-momentum equation in the base axisymmetric flow for practical simplicity. Addition of the ϕ-momentum equation does not require any additional variable, thanks to the stream-surface based finite volume formulation. This new feature of handling swirl velocity can help the internal fan flow passage design. A version of AMIS which can handle swirl velocity jump across the fan has already been written, but is not documented here.

6.2.4 Three-dimensional boundary layer

In the presence of swirl velocity, three-dimensional consideration of the boundary layer is required. There are two possible approaches. The first is a 'quasi-3D' extension of the boundary layer formulations for the infinite swept wing problem. The second is the application of full three-dimensional boundary layer formulations (Mughal [36]). The author feels that the former is a better approach, considering the number of newly introduced variables.

6.2.5 Linearization of a swirling axisymmetric flow

The swirl velocity in the base flow is actually favorable in LAMIS. The non-zero swirl velocity is expected to decrease the round-off errors in the sensitivity calculation of the ϕ-momentum equation. For this, the finite volume formulations of Equation (3.4) - Equation (3.13) need to be reformulated, to include the perturbation flux terms of swirl velocity. Then, S-mometum and RN-momentum equations represent the meridional flow. However, the linearization of such a flow requires the coupling of two sets of perturbation modes mentioned in Chapter 3, which is expected to increase the memory and CPU time requirements by four times.

6.2.6 Geometric perturbation modes

The current set of geometric perturbation modes can not simulate the upper cowl lip advance which is found in most nacelle designs. Defining a geometric perturbation mode in the direction of the x-axis (to be called an axial mode) is recommended for the simulation of three-dimensional nacelle geometries.

6.2.7 Three-dimensional geometry

The capability of the linearized three-dimensional flow prediction around a weakly three-dimensional geometry needs to be demonstrated in the future. Once validated, LAMIS can replace some of the expensive CFD computations which currently require 40-80 hours on a CRAY-YMP.

6.2.8 α and asymmetry of geometry limits

For a better application of LAMIS, the limits of this formulation need to be more thoroughly explored. This can offer the nacelle designers the criteria to decide when to use LAMIS or when to turn the CRAY on.

6.2.9 Improvement of boundary conditions

Improvement of boundary conditions specified by perturbations in the eccentric mode (Figure 3-2) is needed to reduce the level of pressure correction which has adverse effects on the solution. Prescribed eccentric modes close to solution grids are desirable (Figure 5-2).

6.2.10 Constraint of angle mode

Finding proper constraints has been the most difficult task in the present linearization theory development, and not surprisingly, needs improvements for better simulations of vortex sheets or downwash.

6.2.11 Linearized three-dimensional designs

Once a linearized flow solution is obtained, the sensitivities of design modes come as free byproducts. Also, the geometric perturbation modes are already formulated to provide useful design features, like droop. A future demonstration of linearized three-dimensional design capability is recommended for a possible replacement of existing three-dimensional design codes, which have been very expensive.

Bibliography

[1] Anderson, D.A. *et al.* , *Computational Fluid Mechanics and Heat Transfer* , Mc-grawHill, 1984

[2] Arlinger, B.G. " Calculation of Transonic Flow around Axisymmetric Inlets " AIAA Journal, Vol.13, No.12, 1975

[3] Batchelor, G.K., *An Introduction to Fluid Dynamics* , Cambridge University Press, 1967

[4] Cebeci, T. and Bradshaw, P., *Momentum Transfer in Boundary Layers* , McgrawHill, 1977

[5] Bell, R.A. and Cedar, R.D. " An Inverse Method for the Aerodynamic Design of Three-Dimensional Aircraft Engine Nacelles " Proceedings of Third International Conference on Inverse Design Concepts and Optimization in Engineering Sciences, Edited by Dulikravich, G.S., 1991

[6] Belotserkovskii, S. M., *The Theory of Thin Wings in Subsonic Flow* , Plenum Press, 1967.

[7] Boldman, D.R. *et al.* " Evaluation of Panel Code Predictions with Experimental Results of Inlet Performance for a 17-inch Ducted Prop/Fan Simulator " AIAA-91-3354, 1991

[8] Boldman, D.R. *et al.* " Effect of a Rotating Propeller on Separation Angle of Attack and Distortion in Ducted Propeller Inlets " AIAA-93-0017, 1993

[9] Butler, S.F.J. " Aircraft Drag Prediction for Project Appraisal and Performance Estimation " AGARD CP-124, 1973

[10] Caughey, D.A. and Jameson, A. " Accelerated Iterative Calculation of Transonic Nacelle Flowfields " AIAA Journal Vol.15, NO 10, 1977.

[11] Chen, H.C. *et al.* " Flow Simulation for General Nacelle Configurations Using Euler Equations " AIAA-83-0539, 1983

[12] Corson, B.W. *et al.* " Calibration of the Langley 16-Foot Transonic Tunnel with Test Section Air Removal " NASA TR R-423, 1974

[13] Darmofal, D., *A Study of the Mechanisms of Axisymmetric Vortex Breakdown*, Ph.D. thesis, MIT, 1993

[14] Drela, M. " Newton Solution of Coupled Viscous/Inviscid Multielement Airfoil Flows" AIAA-90-1470, 1990

[15] Drela, M. " Viscous and Inviscid Inverse Schemes Using Newton's Method ", AGARD Report AGARD-R-780, *Special Course on Inverse Methods for Airfoil Design for Aeronautical and Turbomachinery Applications* , 1990

[16] Drela, M.and Giles, M.B. " ISES : A Two-Dimensional Viscous Aerodynamic Design and Analysis Code " AIAA-87-0424, 1987

[17] Drela, M., *Two-Dimensional Transonic Aerodynamic Design and Analysis Using the Euler Equations* , Ph.D. thesis, MIT, 1985

[18] Edwards, J.R. and McRae, D.S. " Nonlinear Relaxation/Quasi-Newton Algorithm for the Compressible Navier-Stokes Equations " AIAA Journal Vol.31, No.1, 1993

[19] Giles, M.B., *Newton Solution of Steady Two-Dimensional Transonic Flow*, Ph.D. thesis, MIT, 1985

[20] Gradshteyn, I.S. and Ryzhik, I.M., *Tables of integrals, Series, and Products* , Academic Press, 1965

[21] Graham, R.W. *et al.* " Computational Thermo-Fluid Dynamics Contributions to Advanced Gas Turbine Engine Design " AIAA-85-0083, 1985

[22] Greitzer, E.M. " REVIEW - Axial Compressor Stall Phenomena " ASME Journal of Fluid Eng. Vol.102, pp. 134-151, 1980

[23] Greitzer, E.M. *et al.* " Flow Field Coupling Between Compression System Components in Asymmetric Flow" ASME Journal of Engineering for Power, Vol.100, pp. 618-629, 1978

[24] Hess, J.L. and Smith, A.M.O. " Calculation of Potential Flow about Arbitrary Bodies", pp 1-138 from *Progress in Aeronautical Sciences* Volume 8, Edited by Küchemann, D., Pergamon Press, 1967.

[25] Horlock, J.H., *Actuator Disk Theory* McgrawHill, 1978.

[26] Iek, C. *et al.* " Analysis of an Advanced Ducted Propeller Subsonic Inlet " AIAA-92-0274, 1992

[27] Joo, W., *Intake/Engine Flowfield Coupling in Turbofan Engines*, Ph.D. thesis, Univ. of Cambridge, 1994

[28] Kerrebrock J.L., *Aircraft Engines and Gas Turbines* , MIT Press, 1977

[29] Knight, C. *et al.* " Validation of a Viscous, Incompressible Throughflow Code " AIAA-95-0864, 1995

[30] Küchemann, D. , *Aerodynamics of Propulsion* McgrawHill, 1953

[31] Lahti, D.J. *et al.* " Application of Computational Methods of Large Turbofan Engine Nacelles " AIAA-84-0121, 1984

[32] Langley, M.J. " The Design of Axisymmetric Cowls for Podded Nacelles for High Bypass Ratio Turbofan Engines " R&M No. 3846, 1979

[33] Leicher, S. *et al.* " Investigation of the Flow around a Counter-rotating Shrouded Propfan " Dornier Post, No. 3, 1988, pp 21-23

[34] Liepmann, H.W. and Roshko, A., *Elements of Gasdynamics*, John Wiley&Sons, 1957

[35] Moran, J., *An Introduction to Theoretical and Computational Aerodynamics*, John Wiley&Sons, 1984.

[36] Mughal, B.H., *A Calculation Method for the Three- Dimensional Boundary Layer Equations in Integral Form*, MS. thesis, MIT, 1992

[37] Naik, D.A. *et al.* " Inverse Design of Nacelles Using Multi-Block Navier-Stokes Codes" AIAA-95-1820, 1995

[38] Orkwis, P.D. and Mcrae, D.S. " Newton's Method Solver for the Axisymmetric Navier-Stokes Equations " AIAA Journal Vol.30, No.6, 1992

[39] Pankajashan, R *et al.* " Turbofan Flowfield Simulation Using Euler Equations with Body Forces " AIAA-93-1978, 1993

[40] Re, R.J. and Abeyounis, W.K. " Wind Tunnel Investigation of Three Axisymmetric Cowls of Different Lengths at Mach Numbers " NASA TM-4488, 1993

[41] Re, R.J. " An Investigation of Several NACA 1-Series Axisymmetric Inlets at Mach Number from 0.4 to 1.29 " NASA TM X-2917, 1974

[42] Rossow, C.C., *et al.* " Investigations of Propulsion Integration Interference Effects on a Transport Aircraft Configuration " Journal of Aircraft Vol. 31, No. 5, 1994

[43] Schlichting, H., *Boundary Layer Theory*, McgrawHill, 1968

[44] Seddon, J. and Goldsmith, E.L., *Intake Aerodynamics*, Collins, 1985. Also available in AIAA Education Series.

[45] Smith, L.A. and Campbell, R.L., " Application of a Direct/Iterative Design Method to Complex Transonic Configurations " NASA TP-3234, 1992

[46] Smith, H.J.Jr. " Wake Ingestion Propulsion Benefit " Journal of Propulsion and Power Vol. 9, No.1, 1993.

[47] Sugioka, I., *The Study of Vortex Sheets Using a Panel Method*, M.S. Thesis, MIT, 1985

[48] Swan,W.C. and Sigalla, A. " The Problem of Installing a Modern High Bypass Engine on a Twin Jet Transport Aircraft " AGARD CP-124, 1973

[49] Tan, C.S., *Three-Dimensional Vorticity-Induced Flow Effects in Highly-Loaded Axial Compressor*, Ph.D. thesis, MIT, 1978

[50] Tertervin, N. " A Transformation between Axisymmetric and Two-Dimensional Turbulent Boundary Layers " AIAA Journal, Vol. 8, No.5, 1970

[51] Uenishi K. *et al.* " CFD-Based 3D Turbofan Nacelle Design System " AIAA-90-3081, 1990

[52] Venkatakrishnan, V. " Newton Solution of Inviscid and Viscous Problems " AIAA Journal Vol. 27, No.7, 1989

[53] Volpe, G. " Performance of Compressible Flow Codes at Low Mach Numbers " AIAA Journal Vol. 31, No.1, 1993

[54] White, F.M., *Viscous Fluid Flow* , McgrawHill, 1974

[55] Wigton, L.B. " Application of MACSYMA and Sparse Matrix Technology to Multi-element Airfoil Calculations " AIAA-87-1142-CP, 1987

[56] Wu, C.H. " Three Dimensional Rotating Flow in Transonic Flow in Transonic Turbomachines " ASME Paper 90-GT-13, 1990

[57] Youngren, H.H., *Analysis and Design of Transonic Cascade with Splitter Vanes.*, MS thesis, MIT, 1991

[58] Youngren, H.H. and Bouchard, E.E. *et. al.* " Comparison of Panel Method Formulations and its Influence on the Development of QUADPAN, an Advanced Low-Order Method " AIAA-83-1827, 1983